






Mammalian adipogenesis regulator (Areg) cells use retinoic acid signalling to be non- and anti-adipogenic in age-dependent manner

Magda Zachara^{1,†} , Pernille Y Rainer^{1,†} , Horia Hashimi^{1,†} , Julie M Russeil¹, Daniel Alpern¹ , Radiana Ferrero¹, Maria Litovchenko²  & Bart Deplancke^{1,*} 

Abstract

Adipose stem and precursor cells (ASPCs) give rise to adipocytes and determine the composition and plasticity of adipose tissue. Recently, several studies have demonstrated that ASPCs partition into at least three distinct cell subpopulations, including the enigmatic CD142⁺ cells. An outstanding challenge is to functionally characterise this population, as discrepant properties, from adipogenic to non- and anti-adipogenic, have been reported for these cells. To resolve these phenotypic ambiguities, we characterised mammalian subcutaneous CD142⁺ ASPCs across various experimental conditions, demonstrating that CD142⁺ ASPCs exhibit high molecular and phenotypic robustness. Specifically, we find these cells to be firmly non- and anti-adipogenic both *in vitro* and *in vivo*, with their inhibitory signals also impacting adipogenic human cells. However, these CD142⁺ ASPC-specific properties exhibit surprising temporal phenotypic alterations, and emerge only in an age-dependent manner. Finally, using multi-omic and functional assays, we show that the inhibitory nature of these adipogenesis-regulatory CD142⁺ ASPCs (Aregs) is driven by specifically expressed secretory factors that cooperate with the retinoic acid signalling pathway to transform the adipogenic state of CD142⁻ ASPCs into a non-adipogenic, Areg-like state.

Keywords adipogenesis regulators (Aregs); adipose stem and precursor cells; CD142; differentiation; retinoic acid

Subject Categories Development; Metabolism; Molecular Biology of Disease

DOI 10.15252/emboj.2021108206 | Received 9 March 2021 | Revised 4 July 2022 | Accepted 6 July 2022 | Published online 22 August 2022

The EMBO Journal (2022) 41: e108206

Introduction

Although adipogenesis is one of the best-studied cell differentiation paradigms (Rosen & Spiegelman, 2014), we still have limited

knowledge of the *in vivo* origin and composition of adipose stem and precursor cells (ASPCs; Ferrero *et al.*, 2020). This is partially due to the highly heterogeneous and unstructured nature of adipose tissue depots, which are present in multiple anatomical locations (including subcutaneous and visceral white adipose tissue) and consist of a mixture of different cell types (Cristancho & Lazar, 2011), whose origin and identity differ between distinct fat depots (Cleal *et al.*, 2017). Driven by the resolving power of single-cell RNA-sequencing (scRNA-seq), several studies have recently investigated and confirmed mammalian ASPC heterogeneity (Burl *et al.*, 2018; Hepler *et al.*, 2018; Schwalie *et al.*, 2018; Cho *et al.*, 2019; Gu *et al.*, 2019; Merrick *et al.*, 2019; Spallanzani *et al.*, 2019; Nguyen *et al.*, 2021; Sárvári *et al.*, 2021; Shao *et al.*, 2021). Our own integrative analysis of publicly available scRNA-seq data have thereby allowed the compiling of an ASPC subpopulation consensus based on the fact that the three main identified subpopulations exhibit a remarkable molecular consistency throughout the analysed datasets (Ferrero *et al.*, 2020). These subpopulations include adipose stem-like cells with high expression of *Cd55* and *Dpp4*, pre-adipocyte-like cells with high *Aoc3* and *Icam1* expression, and a rather enigmatic, third population characterised by high *F3* (coding for CD142) and *Clec11a* expression. A hierarchy of these ASPCs has also been proposed with the highly proliferative DPP4⁺ stem-like cells giving rise to the two other subpopulations: ICAM1⁺ and CD142⁺ ASPCs (Merrick *et al.*, 2019), which themselves may be able to interconvert (Merrick *et al.*, 2019; Sárvári *et al.*, 2021). These distinct ASPC subpopulations have been shown to be established as early as post-natal day 12 (P12) in mouse, based on scRNA-seq data (Merrick *et al.*, 2019). At an even earlier developmental stage (P2), immunofluorescence-based *in situ* analyses revealed the presence of anatomically partitioned DPP4⁺ adipose stem-like and ICAM1⁺ pre-adipocyte-like cells (Merrick *et al.*, 2019), however, the presence of CD142⁺ ASPCs in such young mice has not yet been demonstrated.

A great challenge in the field now is to explore whether these molecularly distinct ASPC subpopulations also have different functional properties. In this study, we decided to focus on CD142⁺

1 Laboratory of Systems Biology and Genetics, Institute of Bioengineering, School of Life Sciences, Ecole Polytechnique Fédérale de Lausanne (EPFL) and Swiss Institute of Bioinformatics, Lausanne, Switzerland

2 University College London (UCL) Cancer Institute, London, UK

*Corresponding author. Tel: +41 21 693 18 21; E-mail: bart.deplancke@epfl.ch

†These authors contributed equally to this work as first authors

ASPCs. This is because previous work has defined these cells as being not only non-adipogenic but also anti-adipogenic, which is why they were termed “adipogenesis regulators” (Aregs; Schwalie *et al*, 2018). More recently, independent findings supported the notion that adipose tissue may harbour a negatively regulatory cell type (Lee *et al*, 2019), yet both its identity as well as the underlying molecular mechanisms have so far remained ill-defined (Shamsi *et al*, 2021). The presence of an anti-adipogenic cell population could have tremendous implications with regard to how adipose tissue development and homeostasis is regulated in health and disease. This is why further studies that explore its existence as well as its molecular and functional properties are warranted, especially in light of recent, divergent findings showing that CD142⁺ ASPCs are in fact adipogenic (Merrick *et al*, 2019; Nguyen *et al*, 2021). The reasons for these functional discrepancies between studies have remained unclear but are hypothesised to reflect differences in cell isolation and sorting criteria, antibodies, culturing conditions, distinct lipid quantification strategies, mouse strains, sex and age (Merrick *et al*, 2019; Ferrero *et al*, 2020; Corvera, 2021; Nguyen *et al*, 2021; Dong *et al*, 2022).

Given the importance of resolving the molecular and functional heterogeneity of ASPCs, here, we set out to systematically address these inconsistencies. Our findings validate the molecular and phenotypic robustness of mouse CD142⁺ ASPCs, authenticating these cells as non-adipogenic inhibitors of adipogenesis, a phenotype we showed is conserved *in vivo* and also effective on differentiating ASPCs within the human-derived stromal vascular fraction (SVF) that was isolated from subcutaneous fat. Interestingly however, we demonstrate that these functional properties are age-dependent. Specifically, we show that the molecular identity of CD142⁺ cells is already established before post-natal day 16 (P16), while their non- and anti-adipogenic properties become apparent only 4 weeks after birth. Furthermore, using a diverse range of multi-omic- and functional assays, we provide insights into the molecular mechanisms that control the anti-adipogenic activity of CD142⁺ ASPCs. Particularly, we show that the inhibitory nature of CD142⁺ ASPCs appears to be driven by a set of specifically expressed secretory factors, involving Tissue factor (CD142) itself as well as Matrix Gla protein (MGP), whose actions possibly converge onto the retinoic acid (RA) signalling pathway. These factors/pathways seem to function to render CD142⁺ ASPCs refractory to adipogenesis, while exerting their anti-adipogenic activity by transforming the adipogenic state of CD142⁻ ASPCs into a non-adipogenic, CD142⁺-like state.

Results

CD142⁺ ASPCs are defined by a specific transcriptomic signature and a robust non-adipogenic phenotype

In recent years, numerous studies have dissected white adipose tissue (WAT) composition at the single-cell level (subcutaneous WAT: (Burl *et al*, 2018; Schwalie *et al*, 2018; Cho *et al*, 2019; Merrick *et al*, 2019; Nguyen *et al*, 2021; Shao *et al*, 2021); visceral WAT: (Hepler *et al*, 2018; Spallanzani *et al*, 2019; Sárvári *et al*, 2021; Shao *et al*, 2021); perivascular WAT: (Gu *et al*, 2019)). Together, these studies provide an opportunity to acquire high-resolution insights into ASPC heterogeneity through data integration,

essentially allowing us to validate and possibly expand or revise our initial scRNA-seq-based observations (Schwalie *et al*, 2018). To do so, we integrated data from our own and relevant publicly available mouse subcutaneous adipose tissue scRNA-seq studies (Burl *et al*, 2018; Schwalie *et al*, 2018; Merrick *et al*, 2019) revealing that ASPCs robustly partition among three principal subpopulations in line with earlier observations (Fig 1A and Appendix Fig S1, Ferrero *et al*, 2020). One of these three main ASPC clusters, featuring significantly enriched *F3* (coding for CD142) gene expression, proved to be highly robust and stable across increasing clustering resolution (Fig 1B), indicating that these cells are characterised by a clearly delineated and specific transcriptomic signature.

Given the particular interest in the *F3*⁺ cluster, which was previously identified as representing cells that have inhibitory properties towards adipogenesis (Schwalie *et al*, 2018), we set out to better understand the specific molecular markers of this population. Using the integrative analysis, we identified a set of robust markers that are differentially expressed in each individual scRNA-seq dataset and that are specific to the *F3*⁺ cluster. Combined with the top 20 markers that were detected by bulk RNA-seq as being differentially expressed in CD142⁺ versus CD142⁻ freshly isolated ASPCs in our previous study (Schwalie *et al*, 2018), this resulted in a list of 100 markers that are representative of CD142⁺ ASPCs (top CD142⁺ markers, Appendix Table S1, Materials and Methods). To assess the relevance of this list of gene expression markers, we carried out an in-depth quantitative transcriptomic (BRB-seq, Alpern *et al*, 2019) and proteomic characterisation of freshly isolated FACS-sorted CD142⁺ versus CD142⁻ ASPCs (defined as: SVF Lin⁻(CD31⁻ CD45⁻ TER119⁻)SCA-1⁺CD142⁺ and SVF Lin⁻SCA-1⁺CD142⁻, respectively, Appendix Fig S2, Materials and Methods). The identified top CD142⁺ markers revealed to be specific to CD142⁺ cells both at the transcriptomic and proteomic level (Fig 1C and D, and Appendix Fig S3A and B, Tables S1 and S2). In addition, we found that overall gene and protein expression levels correlated well between all scRNA-seq, bulk RNA-seq and proteomic datasets (Fig 1D, Materials and Methods), indicating that the observed transcriptomic signature of CD142⁺ ASPCs is a reasonable proxy of their protein/functional characteristics. To assess to which extent this signature was affected by culturing or differentiation conditions, we performed bulk RNA-seq of CD142⁻ and CD142⁺ ASPCs post-expansion and post-differentiation (i.e., after exposure to adipogenic medium) as well as a proteomic analysis of expanded, respective populations (Appendix Table S2). Interestingly, we observed that, under these conditions, the expression of many top CD142⁺ markers including *Gdf10*, *Cpe*, *Rbp1*, *F3*, *Bgn*, *Clec11a* and *Mgp* is maintained both at the transcriptomic and/or proteomic level in CD142⁺ ASPCs compared to their CD142⁻ counterparts (Appendix Figs S3C and D, and S4).

To examine the functional properties of these cells, we set out to test the phenotype of CD142⁺ ASPCs across a wide range of experimental conditions and functional assays, aiming to possibly reconcile discrepant findings of CD142⁺ ASPC behaviour (Merrick *et al*, 2019 and Nguyen *et al*, 2021 versus Schwalie *et al*, 2018 and Dong *et al*, 2022). First, we recapitulated our earlier findings (Schwalie *et al*, 2018), showing that the top 5–7% most positive CD142⁺ ASPCs, isolated using the previously employed anti-CD142 antibody, have very low to no adipogenic capacity as compared to CD142⁻ ASPCs when stimulated with a standard white adipogenic differentiation cocktail (Fig 1E and F, and Appendix Fig S5,

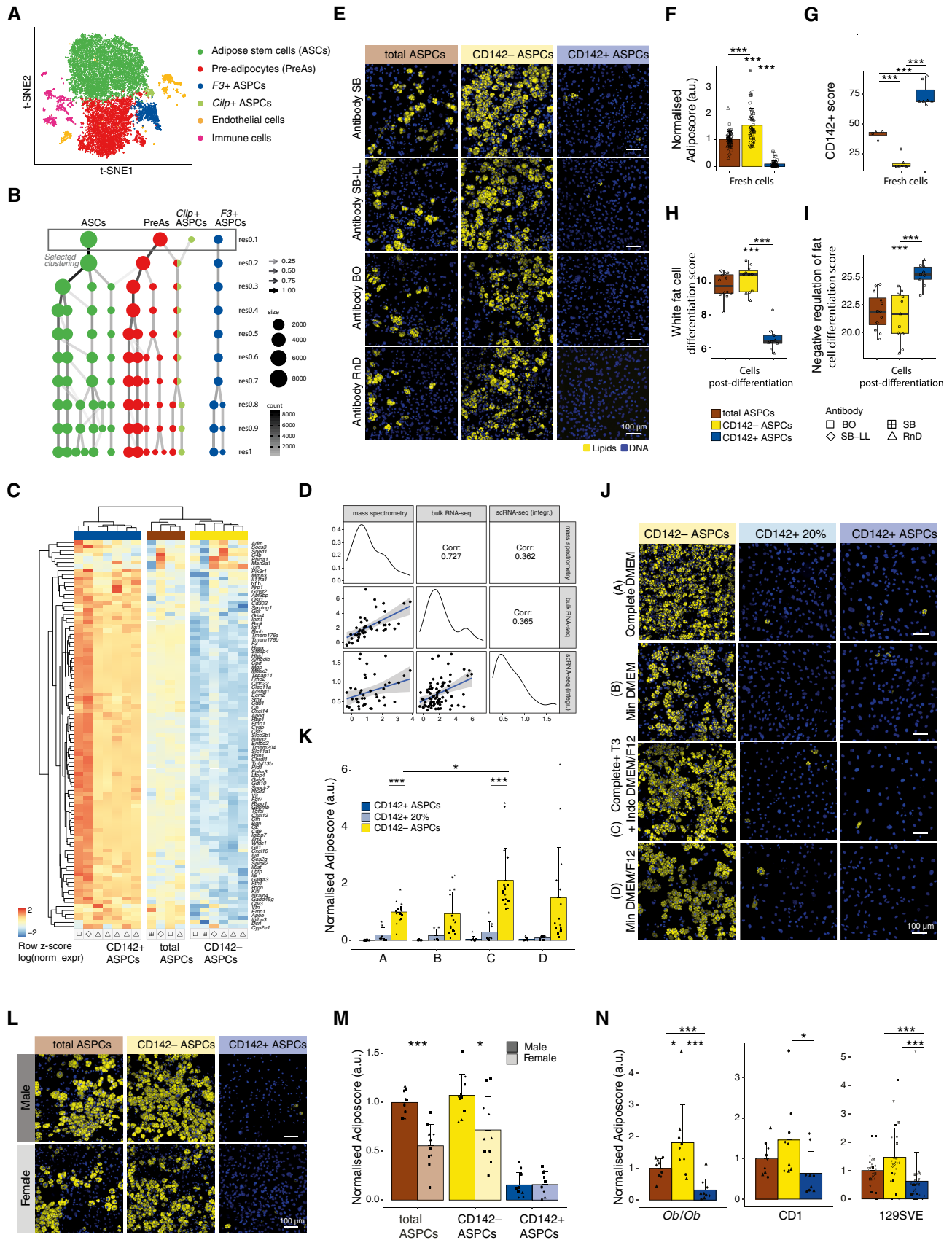


Figure 1.

Figure 1. CD142⁺ ASCs constitute a robust ASC subpopulation defined by a stable non-adipogenic phenotype and a highly specific transcriptomic signature.

- A t-SNE cell map of integrated scRNA-seq datasets (see [Materials and Methods](#)) visualising the main identified subpopulations of mouse subcutaneous ASCs: adipose stem cells (ASCs) in green, pre-adipocytes (PreAs) in red, *F3*(CD142)⁺ ASCs in blue, as well as *Cilp*⁺ ASCs, endothelial and immune cells (see also Appendix Fig S1).
- B Clustering tree of the Seurat-based clustering result of the integrated analysis described in (A), visualising the relationships between clustering at different resolutions of the three main ASC subpopulations as well as *Cilp*⁺ ASCs, demonstrating a high stability of the *F3*(CD142)⁺ ASC cluster.
- C Gene expression heatmap of the top CD142⁺ markers (Appendix Table S1) across bulk RNA-seq samples of freshly isolated total, CD142⁻ and CD142⁺ ASCs; log-normalised expression scaled by row.
- D Correlation of the logFC of top CD142⁺ markers (Appendix Table S1) across scRNA-seq, bulk RNA-seq and mass spectrometry data; logFC was defined as the log₂FC of freshly isolated CD142⁺ over CD142⁻ ASCs for bulk RNA-seq and mass spectrometry, and as the average logFC of *F3*(CD142)⁺ over the remaining cells in scRNA-seq across integrated datasets described in (A) ([Materials and Methods](#)).
- E Representative fluorescence microscopy images of total, CD142⁻ and CD142⁺ ASCs isolated with the use of the respective anti-CD142 antibodies: SinoBiological (SB), SinoBiological-LL (SB-LL), BiOrbyt (BO) and R&D Systems (RnD) (Appendix Figs S2B and S5A, [Materials and Methods](#)), after *in vitro* adipogenic differentiation.
- F Fraction of differentiated cells per ASC type shown in (E), as quantified by the “adiposcore”; marker shapes correspond to different anti-CD142 antibodies used for isolation as indicated, *n* = 9–15, 3–4 biological replicates, 3–5 independent wells for each.
- G Boxplot showing the distribution of the “CD142⁺ score” based on the expression of the top CD142⁺ ASC markers, *n* = 4–7, 1–5 biological replicates, 1–4 independent wells for each (Appendix Table S1, [Materials and Methods](#)).
- H Boxplot showing the distribution of the “white fat cell differentiation score” based on the expression of the genes linked to the GO term “white fat cell differentiation” (GO:0050872), *n* = 9–12, 2 biological replicates, 1–8 independent wells for each ([Materials and Methods](#)).
- I Boxplot showing the distribution of the “negative regulation of fat cell differentiation score” based on the expression of the genes linked to the GO term “negative regulation of fat cell differentiation” (GO:0045599), *n* = 9–12, 2 biological replicates, 1–8 independent wells for each ([Materials and Methods](#)).
- J Representative fluorescence microscopy images of CD142⁻, 20% CD142⁺ and (5–7%) CD142⁺ ASCs isolated following the sorting strategy shown in Appendix Fig S7A, after *in vitro* adipogenic differentiation with the indicated white adipogenic differentiation cocktails ([Materials and Methods](#)).
- K Fraction of differentiated cells per ASC type and differentiation cocktail shown in J, as quantified by the “adiposcore”; marker shapes correspond to different biological replicates, *n* = 8–17, 3–5 biological replicates, 2–5 independent wells for each.
- L Representative fluorescence microscopy images of male- and female-derived total, CD142⁻ and CD142⁺ ASCs, isolated following the sorting strategy shown in Appendix Fig S8A after *in vitro* adipogenic differentiation.
- M Fraction of differentiated cells per ASC type and per sex shown in (L), as quantified by the “adiposcore”; bar colour shading corresponds to male- and female-derived cells as indicated; marker shapes correspond to different biological replicates, *n* = 9–10, 4 biological replicates, 2–3 independent wells for each.
- N Fraction of differentiated cells per ASC type and per mouse genetic background shown in Appendix Fig S10A, as quantified by the “adiposcore”; marker shapes correspond to different biological replicates, *n* = 9–24, 3–5 biological replicates, 3–6 independent wells for each.

Data information: In all images, nuclei are stained with Hoechst (blue) and lipids are stained with Bodipy (yellow); scale bars, 100 μm; bar colours: total ASCs – brown, CD142⁻ ASCs – yellow, CD142⁺ ASCs – blue, 20% CD142⁺ ASCs – turquoise. **P* ≤ 0.05, ****P* ≤ 0.001, pairwise two-sided t-test (F, K, M, N) or one-way ANOVA and Tukey HSD *post hoc* test (G–I), for statistical details see [Materials and Methods](#).

[Materials and Methods](#)). However, since the nature of the antibody may be one of the possible reasons underlying discrepant CD142⁺ cell behaviour read-outs, we tested three more antibodies. While the flow cytometry profiles of the four assessed antibodies differ to a certain extent, the isolated cellular fractions yielded consistent non-adipogenic phenotypic results (Fig 1E and F, and Appendix Figs S5 and S6A, [Materials and Methods](#)). Indeed, when freshly isolated with different antibodies, the respective CD142⁺ ASC samples revealed a consistent transcriptional signature exhibiting a significantly higher expression score based on the top CD142⁺ markers (here named the “CD142⁺ score”, Appendix Table S1, [Materials and Methods](#)) compared to the other tested cellular fractions (total and CD142⁻ ASCs; Fig 1C and G). Finally, the observed non-adipogenic properties of post-differentiation CD142⁺ cells (i.e. post-exposure to a standard adipogenic cocktail) were consistent with the expression profiles of adipogenesis-relevant genes. Specifically, genes involved in “white fat cell differentiation” (GO:0050872) or “negative regulation of fat cell differentiation” (GO:0045599) were significantly lower or higher expressed in CD142⁺ ASCs compared to total or CD142⁻ ASCs, respectively (Fig 1H and I). Moreover, fat and lipid-related terms that were detected as significant by gene set enrichment analysis (GSEA), were negatively enriched in CD142⁺ versus CD142⁻ ASCs (Appendix Fig S6B).

Furthermore, since CD142 surface expression shows a continuum across ASCs (Appendix Fig S6A), it is possible that the stringency of the cell isolation procedure (so far typically 5–7%) has an impact on downstream cell behaviour. To investigate this, we isolated CD142⁺ ASCs using a less stringent gating (~20%, Appendix Fig S7A), yet we did not observe a significant difference in

overall differentiation potential compared to the more stringently isolated cells (Fig 1J and K, and Appendix Fig S7B and C).

Next, we examined the influence of the differentiation medium as it is widely established that adipogenic potential varies as a function of the utilised differentiation cocktail. To do so, we used the standard “complete DMEM” differentiation medium (with insulin, IBMX and dexamethasone) as well as three additional ones (1, “Min DMEM”, with insulin only; 2, “Complete + T3 + Indo DMEM/F12”, with insulin, IBMX, dexamethasone, T3 and indomethacin; 3, “Min DMEM/F12”, with insulin only, [Materials and Methods](#), Schwalie *et al*, 2018; Merrick *et al*, 2019). However, we did not observe notable CD142⁺ ASC differentiation differences across these distinct culturing conditions (Fig 1J and K).

Another source for discrepant cell behaviour could be the sex of the animals. To test this, we isolated CD142⁺ and CD142⁻ ASCs from both male and female mice, revealing that, upon exposure to an adipogenic cocktail, the adipogenic propensity of total and CD142⁻ ASCs was significantly higher (adjusted *P*-value (*P*-adj) < 0.001 and < 0.05, respectively) in males compared to females (Fig 1L and M, and Appendix Fig S8). Furthermore, both male and female CD142⁺ cells were completely refractory to adipogenic differentiation (Fig 1L and M, and Appendix Fig S8). This is in line with transcriptomic results, as our scRNA-seq analysis of male and female cells (Appendix Fig S9A; Schwalie *et al*, 2018) revealed the existence of a clearly delineated *F3*(CD142)⁺ cluster in both sexes with a highly consistent overlap of specific markers (Appendix Fig S9B and C). In addition, the integration of the different publicly available scRNA-seq datasets included cells from mice of different sexes and clearly showed the existence of a robust *F3*⁺

cluster (Burl et al, 2018; Schwalie et al, 2018; Merrick et al, 2019; Fig 1B and Appendix Fig S1).

Finally, we reasoned that the genetic background of analysed mice could also impact the relative difference in adipogenic capacity between the distinct ASPC subpopulations (Fontaine & Davis, 2016). To address this hypothesis, we isolated total, CD142⁻ and CD142⁺ ASPCs from three other mouse strains than C57BL/6J: *Ob/Ob*, CD1 and 129SVE. They were specifically chosen for their relevance in studying obesity or because these strains were used in studies that reported discrepant results regarding the phenotype of CD142⁺ ASPCs (Merrick et al, 2019). However, while the overall differentiation capacity of ASPCs varied across the tested mouse strains, we found that in all strains, CD142⁺ ASPCs have a significantly lower adipogenic potential than their CD142-negative counterparts (Fig 1N and Appendix Fig S10).

Together, these in-depth computational and experimental analyses validate the previously observed molecular identity of CD142⁺ ASPCs and demonstrate the robustness of their non-adipogenic phenotype across a wide range of conditions and experiments.

Age-dependent molecular and phenotypic emergence of bona fide CD142⁺ ASPCs

The findings reported above indicate that CD142⁺ ASPCs constitute a distinct cell population with a well-defined molecular identity and clear non-adipogenic character. However, all of these analyses were performed on cells derived from adult mice, prompting the question whether the observed CD142⁺ cell properties could perhaps be age-dependent. Analysis of publicly available scRNA-seq data of post-natal day 12 (P12) mice revealed a CD142⁺ cluster that shares many of the adult top CD142⁺ markers (Merrick et al, 2019, Appendix Fig S11A and B) and overlaps with adult CD142⁺ ASPCs upon data integration (Appendix Fig S11C and D). Nevertheless, we uncovered that the identity of these P12 *F3*(CD142)⁺ cells, as defined by their “CD142⁺ score” (Appendix Table S1), is significantly less pronounced compared to their adult counterpart (*P*-value < 0.001, Fig 2A and Appendix Fig S11E). To investigate whether this more subtle

molecular identity would also manifest itself at the phenotypic level, we assessed the proportion and adipogenic propensity of different ASPC subpopulations at distinct developmental time points including newborn (P0), 12–17-day-old (P12–17) mice as well as juvenile (4-week-old (4wo)) and adult (7 and 11 wo) animals with these two groups being separated by weaning at post-natal day 21 (P21). Given the overlap between P12 and adult CD142⁺ ASPCs in the scRNA-seq analysis and the specificity of *F3*(CD142) in both age groups (Appendix Fig S11B; Merrick et al, 2019), we used the CD142 marker to enrich for our cellular fractions of interest across ages. We observed significant differences in the proportions of cellular fractions assessed by flow cytometry, with the Lineage negative (SVF Lin⁻) portion being significantly higher (*P*-adj < 0.0001) and the ASPC portion (SVF Lin⁻ SCA-1⁺) significantly lower (*P*-adj < 0.05) in pre-weaning (P0 and P12–17) compared to post-weaning mice (4, 7 and 11 wo; Fig 2B and C, and Appendix Fig S12A). In addition, ASPCs from pre-weaning mice exhibited significantly lower (*P*-adj < 0.01) CD142 cell surface expression compared to post-weaning animals (Fig 2B and C). Indeed, we found that at the gating stringency corresponding to 5% of CD142⁺ cells in adult (11 wo) mice, only 2.5% of newborn (P0) CD142⁺ ASPCs were captured (Fig 2B and C), consistent with the observed gradual decrease of the CD142⁻ ASPC fraction as mice mature (Appendix Fig S12A and B).

Next, we assessed the adipogenic capacity of the different ASPC fractions as a function of age. Using the standard differentiation cocktail (Materials and Methods), we unexpectedly observed that all cellular fractions (total, CD142⁻ and CD142⁺ ASPCs) derived from pre-weaning mice exhibited a remarkable adipogenic propensity with virtually all cells displaying lipid accumulation. However, based on visual inspection, the overall size of the pre-weaning cells and the size of the accumulated lipid droplets tended to be smaller compared to post-weaning cells (Fig 2D). Perhaps most interestingly, pre-weaning-derived CD142⁺ ASPCs gave rise to *in vitro* adipocytes, which is in stark contrast to the marked non-adipogenic properties of their post-weaning counterparts (Fig 2D and E, and Appendix Fig S12C–E). Indeed, we observed that, despite non-negligible variability between independent replicates, the adipogenic

Figure 2. Age-dependent molecular and phenotypic emergence of bona fide CD142⁺ ASPCs.

- A Boxplot showing the distribution of the “CD142⁺ score” (Appendix Table S1) in adult (darker colours) and P12 (lighter colours) ASPCs across the three main ASPC subpopulations (adipose stem cells (ASCs) in green, pre-adipocytes (PreAs) in red and *F3*(CD142)⁺ ASPCs in blue) based on the integration of three single-cell datasets of mouse ASPCs (see Materials and Methods and Appendix Fig S11).
- B FACS-based gating strategy of pre-weaning (new-borns (P0))- and post-weaning (11-week-old (wo))-derived Lin⁻ (defined as CD31⁻ CD45⁻ TER119⁻), SCA-1⁺ (total ASPC), CD142⁻ and CD142⁺ ASPC cellular fractions within the subcutaneous adipose SVF; at least eight biological replicates were performed, shown here is one representative biological replicate.
- C Bar plots showing the normalised parental percentage of pre- and post-weaning indicated cellular fractions; the graph on the right represents the fractions of CD142⁺ ASPCs plotted separately; marker shapes correspond to different biological replicates, *n* = 8–10.
- D Representative fluorescence microscopy images of P0-, P12–17-, 4 wo-, 7 wo- and 11 wo-derived total, CD142⁻ and CD142⁺ ASPCs after *in vitro* adipogenic differentiation.
- E Fraction of differentiated cells per ASPC type shown in (D), as quantified by the “adiposcore”; bar colour shading corresponds to pre- and post-weaning-derived cells as indicated; marker shapes correspond to different biological replicates, *n* = 14–65, 12–13 biological replicates, 2–6 independent wells for each.
- F PCA based on the bulk RNA-seq data of freshly isolated P0-, P16-, 4 wo-, 7 wo- and 11 wo-mice-derived total, CD142⁻ and CD142⁺ ASPCs.
- G Boxplot showing the distribution of the “CD142⁺ score” (Appendix Table S1) across ages and tested cellular fractions (freshly isolated total, CD142⁻ and CD142⁺ ASPCs) showing the age-dependent emergence of the CD142⁺ signature; see colour legend in (F), *n* = 2–5, 2–5 biological replicates, 1 independent well for each.
- H Boxplot showing the distribution of the “CD142⁺ score” (Appendix Table S1) across ages and tested cellular fractions (freshly isolated total, CD142⁻ and CD142⁺ ASPCs) using the log normalised expression corrected for age-driven source of variation; see colour legend in (F), *n* = 2–5, 2–5 biological replicates, 1 independent well for each.

Data information: In all images, nuclei are stained with Hoechst (blue) and lipids are stained with Bodipy (yellow); scale bars, 50 μm; bar colours: total ASPCs — brown, CD142⁻ ASPCs — yellow, CD142⁺ ASPCs — blue; pre-weaning data are represented in lighter shades. **P* ≤ 0.05, ***P* ≤ 0.01, ****P* ≤ 0.001, pairwise two-sided *t*-test (A, C, E, H) or one-way ANOVA and Tukey HSD *post hoc* test (G, null hypothesis: no difference in means across age), for statistical details see Materials and Methods.

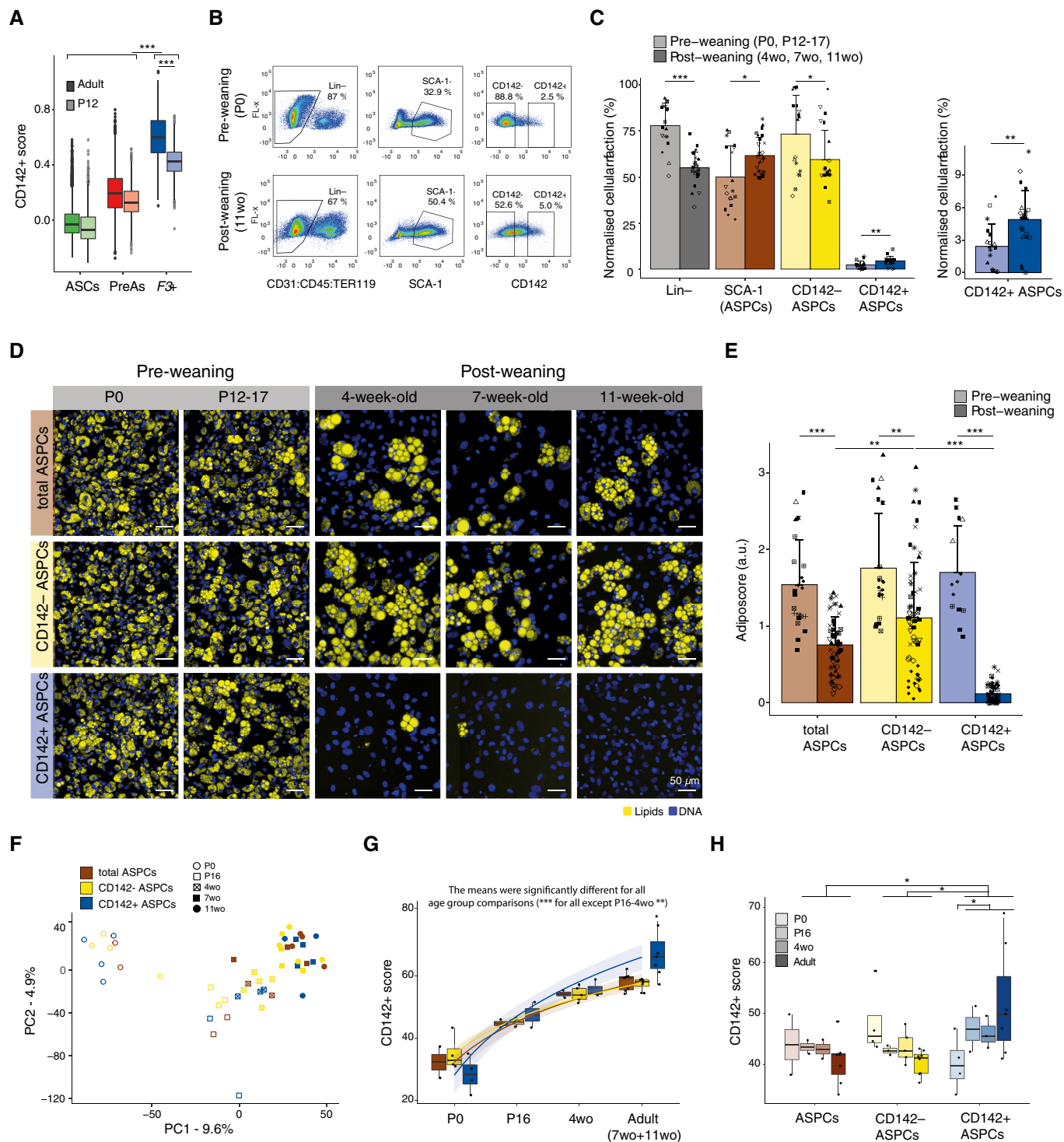


Figure 2.

propensity of total and CD142⁻ ASPCs gradually decreases with age, whereas CD142⁺ ASPCs exhibit a very sharp drop ($P\text{-adj} < 0.0001$) in their ability to give rise to *in vitro* adipocytes between the 16th and 28th (4 wo) day of post-natal development (Fig 2D and E, and Appendix Fig S12C–E).

To further explore this age-dependent functional change of CD142⁺ ASPCs, we performed bulk RNA-seq on freshly isolated ASPC cellular

fractions at different time points after birth (P0, P16, 4, 7 and 11 wo, Appendix Table S2). Analysis of the resulting data revealed that age is the variable that explains the largest variation across samples as they are ordered by this feature along the first principal component (PC1; Fig 2F). GSEA revealed that terms such as “cell fate commitment” (GO:0045165), “mesenchymal cell differentiation/proliferation and development” (GO:0048762, GO:0010463, GO:0014031), “stem cell

differentiation" (GO:0048863), "stem cell population maintenance" (GO:0019827) and cell cycle-related terms are negatively enriched in the genes driving PC1 (Appendix Fig S13A). This suggests that genes linked to these terms are upregulated in freshly isolated young ASPCs, likely reflecting their more naïve "stem" condition. Indeed, all ASPC fractions that were freshly isolated from the newborn burgeoning fat pads expressed substantially higher levels of *Ccnd1* (coding for CyclinD1) and *Dlk1/Pref1*, and lower levels of markers such as *Pdgfrb*, *Cd34* and *Ly6a* (coding for SCA-1) compared to ASPCs from older animals (Appendix Fig S13B–F). Such a signature was proposed to select for a primitive and naïve precursor population (Wang *et al*, 2003; Atanassova *et al*, 2012; Hepler & Gupta, 2017). Interestingly, it has also been shown that foetal and early post-natal ASPCs from murine subcutaneous depots surprisingly express perilipin (*Plin1*) and adiponectin (*Adipoq*) and exhibit highly proliferative and differentiation properties (Hong *et al*, 2015; Hepler & Gupta, 2017), consistent with our observations for newborn-derived ASPCs (Appendix Figs S12C–E, and S13G and H). In contrast, lipid/fat-related terms were enriched in freshly isolated adult ASPCs, implying a molecular state which is less naïve and more committed towards adipogenesis (Appendix Fig S13A). We further found that the "retinol/retinoid metabolic process" (GO:0042572/GO:0001523) gene expression signature is much more prominent in adult-derived ASPCs compared to young ASPCs, which correlates with the decreased adipogenic capacity of adult versus young ASPCs (Appendix Fig S14A and B). In addition to this general increase with age, this same RA-related expression signature was even more pronounced in 4 wo and adult CD142⁺ compared to CD142⁻ ASPCs (Appendix Fig S14C). Interestingly, the "CD142⁺ score" (Appendix Table S1) increased in all the cellular fractions of ASPCs (CD142⁻, CD142⁺ and total ASPCs) in an age-dependent manner (Fig 2G, Appendix Fig S15A). We thereby observed that this set of top markers becomes significantly enriched in CD142⁺ ASPCs (compared to CD142⁻ ASPCs) at P16 and is particularly prominent in adult cells (Appendix Fig S15B–E). Moreover, when we removed the age-driven source of variation from the analysed samples, CD142⁺ ASPCs from all developmental time points, except P0, were marked by a relative and substantial increase of the "CD142⁺ score" compared to the other assessed fractions (all ages, total and CD142⁻ ASPCs), while being once again more pronounced in adults, reflecting the results from our scRNA-seq analysis of P12- and adult-derived ASPCs (Fig 2A; Merrick *et al*, 2019). This increase was accompanied by a gradual decrease of the "CD142⁺ score" in all CD142⁻ ASPCs with age (Fig 2H).

Together, these findings suggest that ASPCs and their considered subpopulations are molecularly and phenotypically naïve at birth, after which they gradually acquire their respective properties throughout the early post-natal developmental stages. Furthermore, the definite "CD142⁺-specific expression signature" appears to emerge in CD142⁺ ASPCs before P16, followed by the manifestation of their completely non-adipogenic phenotype by post-natal week 4.

CD142⁺ ASPC-dependent adipogenic inhibition and mediating factors

The findings above validate the previously described molecular identity of CD142⁺ ASPCs, provide additional evidence as to the robustness of their non-adipogenic character, and add the interesting dimension of this phenotypic property emerging with age.

Importantly, our results also corroborate the notion that adult CD142⁺ ASPCs are not only non-adipogenic, but also anti-adipogenic. This is because adult CD142⁻ ASPCs reproducibly exhibit a greater adipogenic propensity than total ASPCs (Figs 1E and F, and 2D and E), suggesting that the presence of CD142⁺ ASPCs dampens the adipogenic capacity of their CD142⁻ counterparts.

To better understand the molecular mechanisms underlying the inhibitory function of CD142⁺ ASPCs, we first re-explored the anti-adipogenic nature of these cells *in vitro* using a transwell set-up allowing specific ASPC subpopulations to be co-cultured without cell-to-cell contact (Materials and Methods). These experiments revealed that CD142⁻ ASPCs co-cultured with CD142⁺ ASPCs show a significantly decreased capacity to generate adipocytes (*P*-value < 0.01) compared to CD142⁻ ASPCs cultured on their own (Fig 3A and B). We then investigated whether CD142⁺ ASPCs also retain their anti-adipogenic properties *in vivo*. Using a matrigel-based implantation model, we have previously shown that CD142⁺-depleted SVF and CD142⁻ ASPCs exhibit increased adipogenesis *in vivo* compared to total SVF or ASPCs (Schwalie *et al*, 2018). Here, we aimed to complement these studies by reintroducing isolated CD142⁺ ASPCs into a CD142⁻ ASPC population in pre-defined proportions and monitor their impact on fat cell formation. To do so, we subcutaneously injected Matrigel plugs containing only CD142⁻ ASPCs on the one hand and, on the other, CD142⁻ ASPCs to which 10–20% of isolated CD142⁺ ASPCs were added. After 3 weeks of high-fat diet to induce adipogenesis, we performed histological analysis on the excised plugs, observing that the number of mature adipocytes that had been formed in the plugs containing 10–20% CD142⁺ ASPCs was significantly lower than that in CD142⁻-devoid plugs for both male and female mice (Fig 3C and D, and Appendix Fig S16A), thus confirming the anti-adipogenic nature of CD142⁺ ASPCs *in vivo*. This difference was much greater than could have been expected from the simple decrease in the proportion of highly adipogenic CD142⁻ ASPCs, suggesting that the CD142⁺ ASPCs exert an inhibitory effect in the plug. Interestingly, the mean adipocyte size also diminished by around 25% in the presence of CD142⁺ ASPCs (Fig 3C), suggesting that the latter might also play a role in controlling the growth of maturing adipocytes.

To molecularly support the observed inhibitory capacity of CD142⁺ ASPCs, we performed bulk RNA-seq of differentiated CD142⁻ ASPCs and differentiated CD142⁻ ASPCs that were co-cultured with CD142⁺ ASPCs (Appendix Table S2). Consistent with our phenotypic observations, CD142⁻ ASPCs cultured alone showed a significantly higher expression of genes related to "white fat cell differentiation" (GO:0050872; Appendix Fig S16B), while key genes linked to the "negative regulation of fat cell differentiation" (GO:0045599) were up-regulated in CD142⁻ ASPCs that were co-cultured with CD142⁺ cells (Fig 3E). These results recapitulate CD142⁺ ASPCs' previously reported capacity to inhibit adipogenesis through paracrine signalling (Schwalie *et al*, 2018). Together with a recent, independent report showing a comparable capacity of CD142⁺ stromal cells in muscle (Camps *et al*, 2020), we therefore decided to reintroduce the original "Adipogenesis regulators" (Aregs) nomenclature to conceptually define CD142⁺ ASPCs.

Next, we wondered whether the anti-adipogenic signals that are produced by Aregs could also impact human ASPC differentiation. To investigate this, we set up a transwell experiment allowing

human SVF that was derived from subcutaneous fat depots, and thus containing the ASPCs, to be exposed to the secretome of the mouse-derived total, CD142⁻, or CD142⁺ ASPC fractions. We found that significantly less mature adipocytes were formed when human ASPCs were co-cultured with CD142⁺ ASPCs compared to when they were co-cultured with CD142⁻ ASPCs (Fig 3F and G, and Appendix Fig S17). These findings indicate that human SVF cells are sensitive to the anti-adipogenic effect of Aregs and suggest that the underlying molecular response machinery might be conserved in human.

To uncover these anti-adipogenic signals, we mined the generated transcriptome and proteome data to identify Areg-specific secreted factors. This resulted in a stringent set of highly Areg-specific candidates including *F3* (coding CD142) itself, *Mgp*, *Gdf10*, *Clec11a*, *Cpe* and *Bgn* (Fig 3H, Appendix Tables S1 and S2, and Materials and Methods). To assess the inhibitory potential of these factors, we treated CD142⁻ ASPCs with various concentrations of recombinant candidate proteins, aiming to mimic the physiological presence of Aregs. Similar to the above-described experiments, the extent of adipogenesis was inherently variable across distinct batches, assays

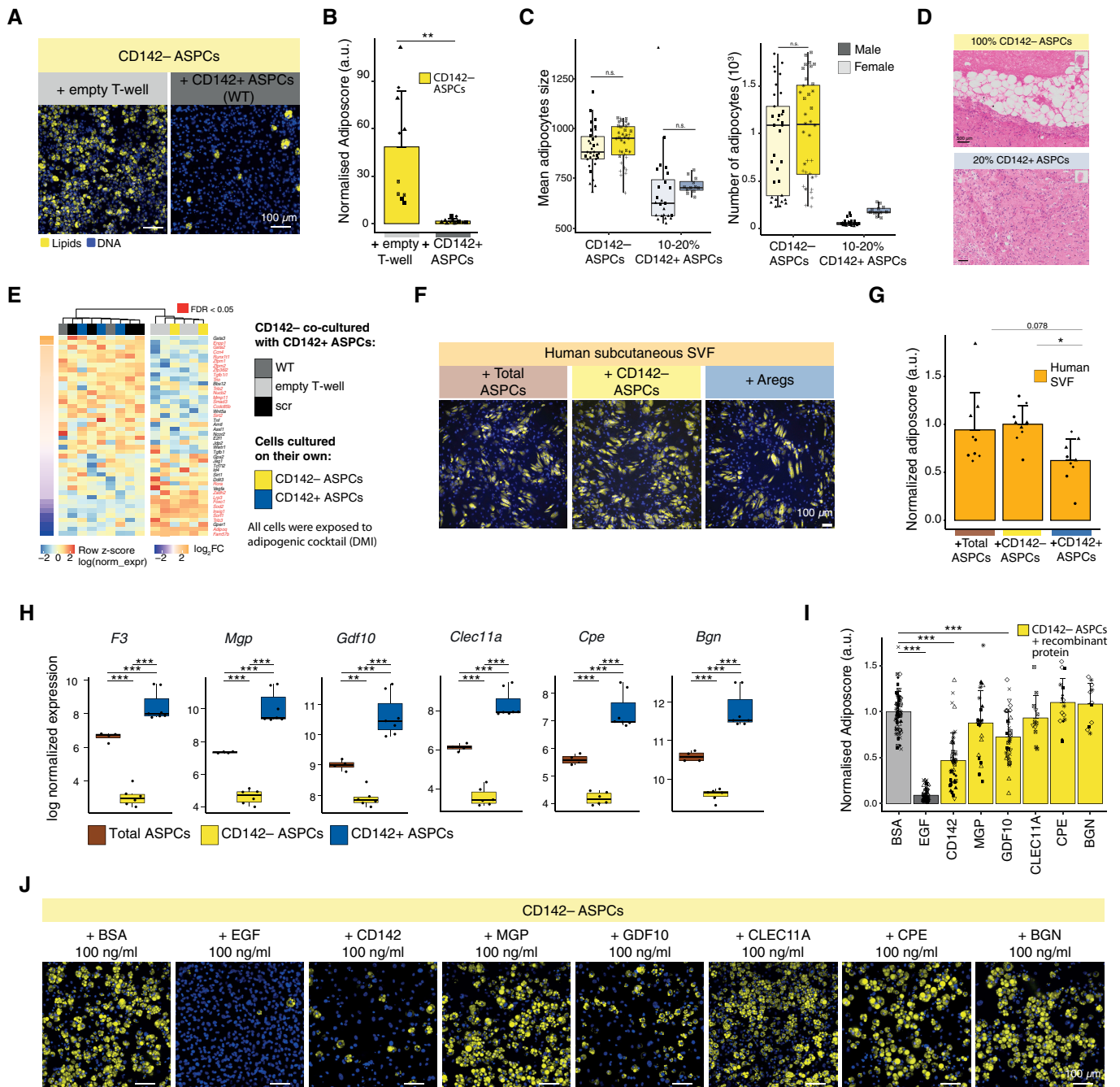


Figure 3.

Figure 3. CD142⁺ ASPC (Areg)-specific candidates and their involvement in adipogenic inhibition.

- A Representative fluorescence microscopy images of CD142⁻ ASPCs co-cultured with an empty transwell (T-well) or with wild-type (WT) CD142⁺ ASPCs after *in vitro* adipogenic differentiation.
- B Fraction of differentiated CD142⁻ ASPCs co-cultured with an empty transwell (T-well) or with wild-type CD142⁺ ASPCs (non-treated or treated with control scrambled siRNA) after *in vitro* adipogenic differentiation and as quantified by the “adiposcore”; marker shapes correspond to different biological replicates, $n = 10$, 4 biological replicates, 2–3 independent wells for each.
- C Mean size or number of quantified adipocytes in matrigel plugs which were implanted into the subcutaneous adipose depot after 3 weeks of high-fat diet. The plugs were injected with either only CD142⁻ ASPCs, or with a mix containing 10–20% of CD142⁺ ASPCs. Markers correspond to different biological replicates, $n = 12$ –36, 1–3 biological replicates (6 mice in total), 9–12 slides for each.
- D Representative histology images of matrigel implant cuts after fixation with 4% PFA and dehydration of plugs injected with CD142⁻ ASPCs (top) or 80% of CD142⁻ ASPCs and 20% of CD142⁺ ASPCs (bottom). Both images are of plugs dissected from a female mouse after matrigel injection and 3 weeks on high-fat diet. In pink: matrigel, in white: adipocytes, scale bar = 500 μm , staining haematoxylin and eosin.
- E Expression heatmap listing genes linked to “negative regulation of fat cell differentiation” (GO:0045599) across bulk RNA-seq samples of CD142⁺ and CD142⁻ ASPCs after adipogenic differentiation; the genes are ordered from top to bottom by the $\log_2\text{FC}$ of CD142⁺ over CD142⁻ ASPCs after adipogenic differentiation; significantly differentially expressed genes (FDR < 0.05) are coloured in red; log normalised expression scaled by row; T-well – transwell, scr – scrambled siRNA (control).
- F Representative fluorescence microscopy image of human-derived stromal vascular fraction (SVF), containing the ASPCs, after *in vitro* adipogenic differentiation when co-cultured with total, CD142⁻ or CD142⁺ mouse ASPCs.
- G Fraction of differentiated human-derived SVF, containing the ASPCs co-cultured with total, CD142⁻ or CD142⁺ mouse ASPCs after *in vitro* adipogenic differentiation (Materials and Methods) shown in (E); marker shapes correspond to different biological replicates, $n = 9$, 3 biological replicates, 3 independent wells for each.
- H Bulk RNA-seq-derived expression plots of CD142⁺ ASPC (Areg) markers coding for secreted proteins that were selected for downstream validation: *F3* (coding for CD142), *Mgp* (coding for Matrix Gla protein, MGP), *Gdf10* (GDF10), *Clec11a* (CLEC11A), *Cpe* (Carboxypeptidase E, CPE) and *Bgn* (Biglycan, BGN), $n = 4$ –7, 1–5 biological replicates, 1–4 independent wells for each.
- I Fraction of differentiated adult-derived CD142⁻ ASPCs, as quantified by the “adiposcore”, treated with the indicated recombinant proteins shown in (J); marker shapes correspond to different biological replicates, $n = 11$ –59, 2–10 biological replicates, 3–9 independent wells for each.
- J Representative fluorescence microscopy images of adult-derived CD142⁻ ASPCs after *in vitro* adipogenic differentiation; the induction cocktail was supplemented with recombinant proteins corresponding to the selected Areg-specific candidates: CD142, MGP, GDF10, CLEC11A, CPE and BGN at 100 ng/ml (Materials and Methods).

Data information: In all images, nuclei are stained with Hoechst (blue) and lipids are stained with Bodipy (yellow); scale bars, 100 μm , bar colours: total ASPCs – brown, CD142⁻ ASPCs – yellow, CD142⁺ ASPCs (Aregs) – blue, recombinant BSA or DMSO treatment (negative controls) – light grey, recombinant EGF treatment (positive control) – dark grey. * $P \leq 0.05$, ** $P \leq 0.01$, *** $P \leq 0.001$, pairwise two-sided t-test (B, C, G, I) or one-way ANOVA and Tukey HSD *post hoc* test (H), for statistical details see Materials and Methods.

and cell populations. Nevertheless, both recombinant CD142 (P -adj < 0.001) and GDF10 (P -adj < 0.001) significantly inhibited adult-derived CD142⁻ ASPC adipogenesis at a concentration of 100 ng/ml, while recombinant MGP inhibited adipogenesis at 1 $\mu\text{g}/\text{ml}$ (P -adj < 0.001; Fig 3I and J, Appendix Figs S18 and S19, and Materials and Methods). Interestingly, P0-derived CD142⁻ ASPCs appeared to a large extent refractory to such an inhibition, illustrated by a much less striking decrease in the extent of adipogenesis upon treatment with recombinant EGF, a well-established adipogenesis inhibitor (Harrington *et al*, 2007) that was used as a positive control (Appendix Fig S20, Materials and Methods). Nevertheless, we still observed a significant decrease in the extent of adipogenesis when newborn CD142⁻ ASPCs were exposed to recombinant CD142, GDF10, MGP and BGN (P -adj < 0.01, < 0.01, < 0.001 and < 0.05, respectively), with MGP now exerting the most pronounced inhibitory effect on differentiating newborn-derived CD142⁻ ASPCs (Appendix Fig S20).

To further validate the involvement of *F3* (CD142), *Mgp* and *Gdf10* in mediating the anti-adipogenic nature of Aregs, we first knocked each of these genes down in adult CD142⁺ and total ASPCs in an siRNA-dependent manner (for an assessment of knockdown (KD) efficiency, see Appendix Fig S21) and examined its impact on adipogenesis. We observed that for each of these three genes, their respective KD lead to a variable but consistent increase of adipogenic propensity both in CD142⁺ and total ASPCs, with more pronounced effects in the total ASPC population (Appendix Fig S21, Materials and Methods). Indeed, we found that siRNA-mediated changes in lipid accumulation in CD142⁺ ASPCs were small, suggesting an inherent inability of these cells to give rise to adipocytes, at least in the imposed culturing conditions. Given the Areg-specific (among ASPCs) expression of *F3*, *Mgp*

and *Gdf10* genes, we interpret the increase of total ASPC adipogenesis upon KD of these respective genes as a consequence of specifically inactivating Areg function. To support this interpretation in a more rigorous way, we performed transwell assays, allowing CD142⁻ ASPCs to be exposed to the secretome of CD142⁺ ASPCs in which the respective candidate factors were knocked down. We observed that inactivating each of these three genes caused an increased adipogenesis of co-cultured CD142⁻ ASPCs compared to control (scrambled (scr) siRNA), suggesting that they are indeed involved in mediating the anti-adipogenic activity of Aregs. However, while we observed that *F3* and *Mgp* KD caused a significant increase in overall differentiation of CD142⁻ ASPCs (P -adj < 0.01 and < 0.01, respectively, Fig 4A and B, Appendix Fig S21H and I), *Gdf10* KD had a lower effect (P -adj = 0.052).

To further characterise the molecular mechanism(s) underlying the observed Areg-mediated inhibitory signalling, we profiled the transcriptomes of CD142⁻ ASPCs responding to CD142⁺ ASPCs, whose activity was modulated via individual KDs (Appendix Table S2). We observed that the respective gene expression profiles reflected the image-based differentiation results to a great extent, with adipogenic propensity differences driving the first principal component (PC1) and correlating with the overall transcriptomics-based “white fat cell differentiation score” (GO:0050872; Fig 4C, Appendix Fig S22A and B). Interestingly, distinct CD142⁻ ASPC samples grouped as a function of how effectively they were impacted by CD142⁺ ASPC signalling, forming two clusters corresponding to “active Areg” signalling (CD142⁻ ASPCs co-cultured with si*Gdf10*, as well as WT and scr Aregs) and what we interpret as “dysfunctional Areg” signalling (co-cultured with si*F3*, si*Mgp* Aregs and with an empty transwell, Fig 4A–C). Furthermore, we found that in CD142⁻ ASPCs that responded to “active

Aregs”, the expression of most top CD142⁺ markers (i.e., Areg-specific markers) including *F3*, *Bgn*, *Rbp1*, *Osr1*, *Cpe*, *Mgp* and *Gdf10* is higher compared to the other CD142⁻ ASPC samples, suggesting that the molecular state of CD142⁻ ASPCs that were exposed to “active Aregs” became itself more Areg-like (Fig 4D and Appendix Fig S22C). To test this hypothesis, we integrated transcriptomic profiles of CD142⁻ and CD142⁺ ASPCs that were on their own exposed to an adipogenic cocktail for 6–8 days (Appendix Table S2) into the analysis of bulk RNA-seq data derived from CD142⁻ ASPCs that were co-cultured with distinct KD CD142⁺ ASPCs. Remarkably, post-differentiation CD142⁺ and CD142⁻ ASPCs fell into the two distinct clusters corresponding to

“active” and “dysfunctional Aregs” respectively, indicating that the CD142⁺ ASPCs were transcriptionally similar to CD142⁻ ASPCs that were exposed to “active Aregs” (Fig 4D and E, and Appendix Fig S22D). Furthermore, we observed a strong anti-correlation between the Areg versus “white fat cell differentiation” signatures inferred from all the considered samples (Fig 4F, Appendix Fig S22A and C, and Table S1). Specifically, we found that the expression of most top Areg markers, and particularly those of all tested candidates, strongly anti-correlate with the “white fat cell differentiation score” (Fig 4G and Appendix Fig S22E, Materials and Methods).

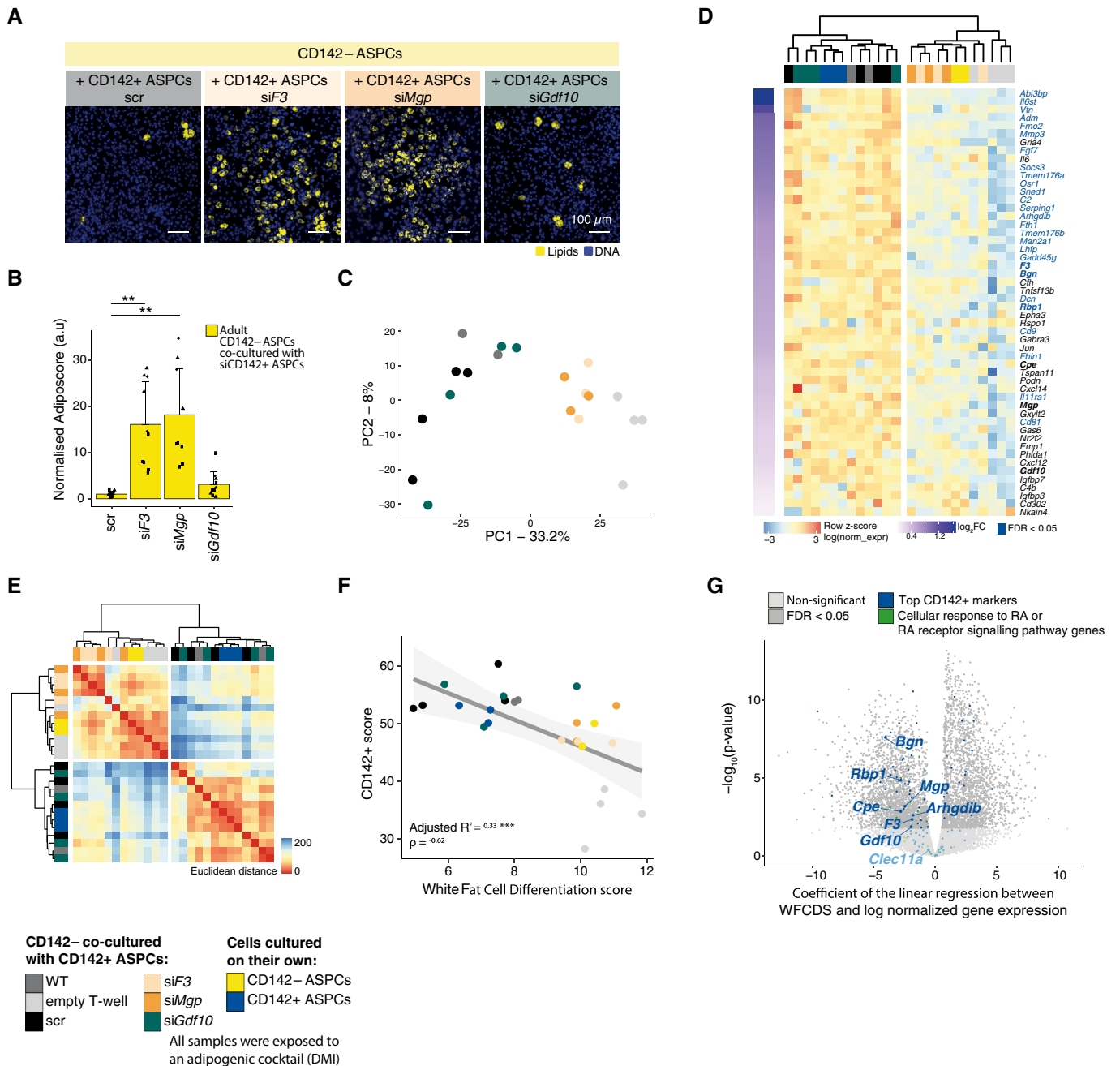


Figure 4.

Figure 4. Molecular (auto-)regulation of CD142⁺ ASPC (Areg)'s inhibitory activity.

- A Representative fluorescence microscopy images of CD142⁻ ASPCs, co-cultured with CD142⁺ ASPCs (Aregs) carrying control (scrambled (scr)) or siRNA-mediated knockdowns of selected CD142⁺ ASPC (Areg)-specific candidate genes: *F3*, *Mgp* and *Gdf10* after adipogenic differentiation (i.e., after exposure to an adipogenic cocktail, [Materials and Methods](#)).
- B Fraction of differentiated CD142⁻ ASPCs, as quantified by the “adiposcore”, co-cultured with CD142⁺ ASPCs (Aregs) subjected to specific knockdowns (or scr siRNA control), as indicated in (A); marker shapes correspond to different biological replicates, $n = 10$, 4 biological replicates, 2–3 independent wells for each.
- C PCA based on bulk RNA-seq data of CD142⁻ ASPCs co-cultured with CD142⁺ ASPCs (Aregs) subjected to specific knockdowns as indicated in (A); see colour legend at the bottom of the figure.
- D Expression heatmap of top CD142⁺ markers (i.e., Areg markers, Appendix Table S1) with a positive log₂FC when performing differential expression analysis between CD142⁻ ASPCs that were exposed to “active Aregs” (WT, scr, si*Gdf10*) versus CD142⁻ ASPCs that were exposed to “dysfunctional Aregs” (si*F3*, si*Mgp*) across the bulk RNA-seq of the same samples and of CD142⁻ and CD142⁺ ASPCs after exposure to an adipogenic cocktail; genes are ordered from the highest (top) to the lowest (bottom) log₂FC; significantly differentially expressed genes (FDR < 0.05) are coloured in blue; Areg candidates are highlighted in bold; log normalised expression scaled by row; see colour legend at the bottom of the figure.
- E Heatmap showing the Euclidian distance of the transcriptomic data of CD142⁻ ASPCs co-cultured (via transwell) with distinct CD142⁺ ASPC knockdown types or controls as well as CD142⁺ or CD142⁻ ASPCs post-differentiation, calculated on the five first principal components of the PCA shown in Appendix Fig S23D.
- F Correlation of “white fat cell differentiation score” versus “CD142⁺ score”; see colour legend at the bottom of the figure.
- G Volcano plot showing the coefficient of the linear regression performed between “white fat cell differentiation score” (WFCDS) and log normalised gene expression (WFCDS ~ log(normalised expression)) (x-axis) versus the $-\log_{10}(P\text{-value})$ (y-axis); top CD142⁺ markers (i.e., Areg markers, Appendix Table S1) are highlighted in blue and genes linked to “cellular response to RA” (GO:0071300) and “RA receptor signalling pathway” (GO:0048384) terms in green.

Data information: In all images, nuclei are stained with Hoechst (blue) and lipids are stained with Bodipy (yellow); scale bars, 100 μm . * $P \leq 0.05$, ** $P \leq 0.01$, *** $P \leq 0.001$, pairwise two-sided t -test (B), for statistical details see [Materials and Methods](#).

Overall, our findings show the importance of CD142 and MGP in the inhibitory effect of Aregs. They also point to a strong association between Areg marker (Appendix Table S1) expression (especially of the tested candidates) and the inability of ASPCs to undergo adipogenic differentiation.

Aregs' anti-adipogenic properties are mediated by the retinoic acid pathway

Among the Areg-specific factors, we also identified a few retinoic acid (RA)-related genes including *Rbp1*, *Aldh1a2*, *Epha3* and *Osr1* (Fig 5A, Appendix Fig S23A and Table S1, [Materials and Methods](#)). This is further illustrated by the significant enrichment of the GO term “retinol metabolic process” (GO:0042572; with retinol being a precursor of RA) in transcriptomic and proteomic data from freshly isolated CD142⁺ compared to CD142⁻ ASPCs (Fig 5B, and Appendix Fig S23B and C). We also uncovered that transcriptomic data from cultured CD142⁺ ASPCs treated with standard white adipogenic cocktail is enriched for the “cellular response to RA” (GO:0071300) and “RA receptor signalling pathway” (GO:0048384) terms compared to CD142⁻ ASPCs post-differentiation (Fig 5C, Appendix Figs S23D and E, and S24A). Remarkably, using the same transcriptomic data from CD142⁻ ASPCs exposed to KD Aregs described in Fig 4, we observed that the “cellular response to RA” (GO:0071300) and “RA receptor signalling pathway” (GO:0048384) terms were also enriched in CD142⁻ ASPCs subjected to “active Areg” signalling (Fig 5C, and Appendix Fig S24B and C) compared to cells subjected to “dysfunctional” Aregs. The expression of the genes involved in these two latter GO terms was anti-correlated with our “white fat cell differentiation score” (Figs 4G and 5D) and positively correlated with the “CD142⁺ score” (Fig 5D and E, Appendix Fig S22A, F and G). This suggests that the expression of Areg markers could be (at least partially) regulated by RA when exposed to adipogenic stimuli. To further explore this hypothesis, we treated CD142⁻ ASPCs with RA, using concentrations ranging from 0.001 to 100 μM ([Materials and Methods](#)). First, as previously shown in 3T3 cells (Murray & Russell, 1980), we observed a significant decrease ($P\text{-adj} < 0.001$) in the extent of adipogenesis (from 0.1 μM

RA, Appendix Fig S25). We then performed bulk RNA-seq of CD142⁻ ASPCs treated with RA, or EGF (as a control), to compare their respective transcriptomes to the ones of Aregs and of CD142⁻ ASPCs co-cultured with “active Aregs”. This analysis revealed that the two latter were transcriptionally more similar to CD142⁻ ASPCs treated with RA than those treated with EGF (Appendix Fig S26), a similarity that can therefore not solely be explained by the low expression of adipo-related genes. In addition, we observed that Aregs, and CD142⁻ ASPCs exposed to “Active” Areg signalling, exhibited, upon exposure to differentiation cocktail, remarkably coherent transcriptional dynamics of a number of genes and pathways that were previously reported to be involved in the RA-mediated inhibition of adipogenesis, a pattern of expression supported by the analysis of CD142⁻ ASPCs treated with RA (Appendix Fig S27, Schwartz *et al*, 1996; Boney *et al*, 1998; MacDougald & Mandrup, 2002; Goldstein *et al*, 2009; Lee *et al*, 2011; Kim *et al*, 2013; Sagara *et al*, 2013; Takahashi *et al*, 2015; Wang *et al*, 2017). Furthermore, next to an impaired adipogenic capacity (Appendix Fig S25), RA-treated CD142⁻ ASPCs exhibited a strikingly consistent transcriptomic signature, with a number of highly specific Areg markers being regulated by RA in a concentration-dependent manner. Indeed, we observed that the expression of *F3* and *Mgp* but also of *Cpe*, *Gdf10*, *Bgn*, *Clec11a*, and other Areg-specific genes are gradually upregulated by increasing concentrations of RA (Fig 5F and Appendix Fig S28). However, for a number of genes (*F3*, *Mgp*, *Bgn*, *Clec11a*), RA administered at concentrations higher than 10 μM tended to reverse this up-regulation, potentially pointing to an effective RA concentration range (0.01–1 μM) that may be physiologically relevant for the Areg-dependent inhibition of adipogenesis. Overall, these results support the involvement of RA in regulating the expression of Areg markers, and notably secretory factors such as CD142, MGP and GDF10, which appear involved in mediating the inhibitory capacity of Aregs.

To experimentally validate the importance of RA in mediating Aregs' inhibitory capacity, we treated ASPCs with different RA signalling antagonists, aiming to either block the physiological production of RA (DEAB, [Materials and Methods](#)) or modulate the activity of RA-activated transcription factors, notably Retinoid X receptors,

RXRs and Retinoic Acid Receptors, RARs (HX or AGN and BMS, respectively, [Materials and Methods](#)). More specifically, we performed transwell assays in which only transwell-deposited Aregs

were treated with the compounds after which we examined the effect of these antagonists (via Aregs) on CD142⁻ ASPC differentiation. Remarkably, while the extent of differentiation tended to be

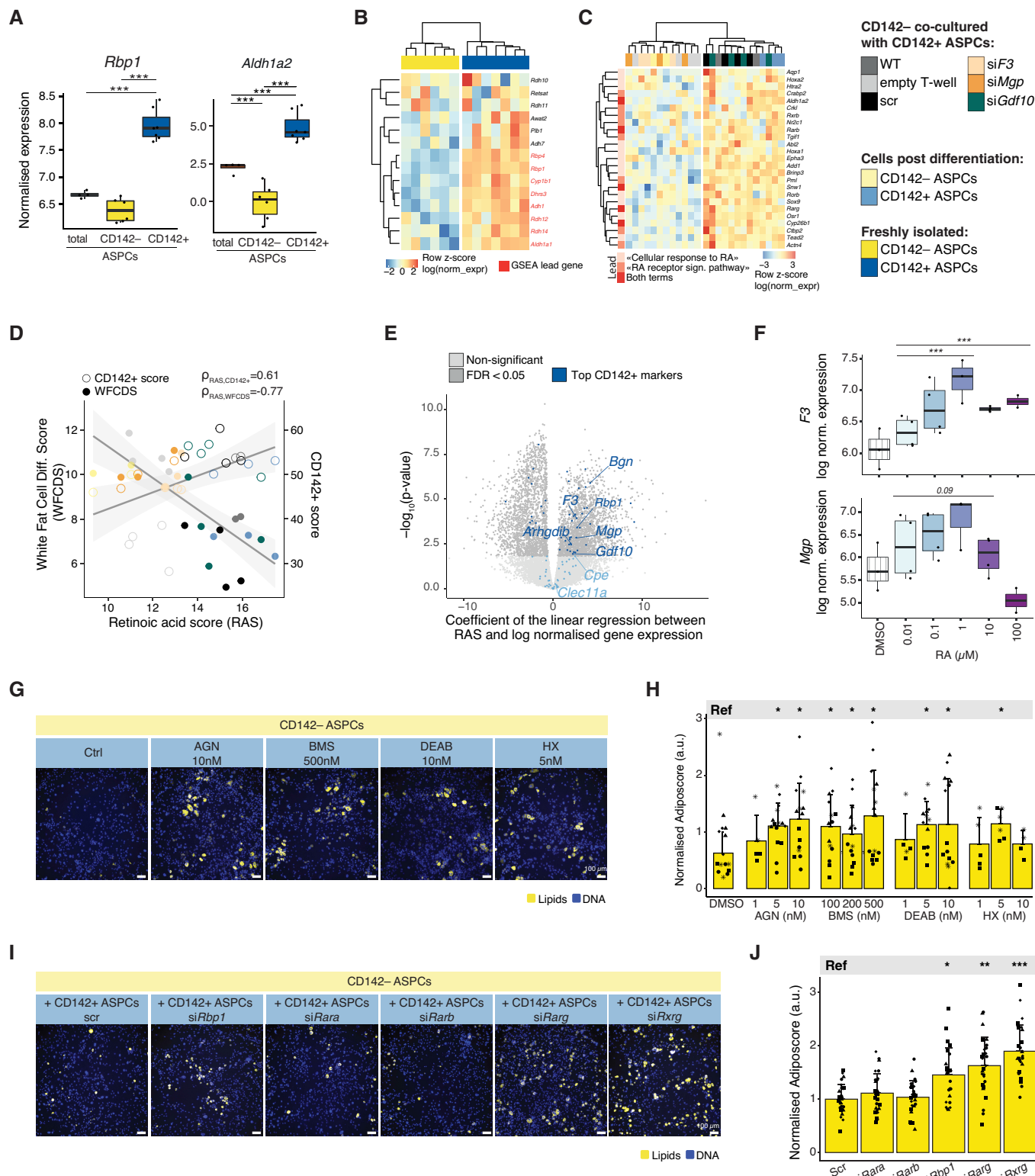


Figure 5.

Figure 5. RA signalling modulates Aregs' anti-adipogenic property.

- A Bulk RNA-seq-derived expression plots of *Rbp1* (Retinol-binding protein 1) and *Aldh1a2* (coding for Retinal dehydrogenase, RALDH2) in freshly isolated total, CD142⁻ and CD142⁺ ASPCs, $n = 4-7$, 1-5 biological replicates, 1-4 independent wells for each.
- B Expression heatmap listing genes linked to "retinol metabolic process" (GO:0042572) across bulk RNA-seq samples of freshly isolated CD142⁻ and CD142⁺ ASPCs; genes identified as lead by GSEA (Materials and Methods) are coloured in red; log normalised expression scaled by row.
- C Expression heatmap of the lead genes identified by GSEA of the significantly enriched terms "cellular response to RA" (GO:0071300) and "RA receptor signalling pathway" (GO:0048384); GSEA identified these two terms as enriched when performed on the genes driving PC1 shown in Fig 4C; see colour legend at the bottom of the figure.
- D Correlation plot of "RA score" (RAS; based on the expression of genes linked to "cellular response to RA" (GO:0071300) and "RA receptor signalling pathway" (GO:0048384)) versus "CD142⁺ score" (Appendix Table S1) or "white fat cell differentiation score" (WFCDs; GO:0050872).
- E Volcano plot showing the coefficient of the linear regression performed between "RA score" (RAS; based on the expression of genes linked to "cellular response to RA" (GO:0071300) and "RA receptor signalling pathway" (GO:0048384)) and log normalised gene expression (RAS ~ log(normalised expression)) (x-axis) versus the $-\log_{10}(P\text{-value})$ (y-axis); top CD142⁻ markers (i.e., Areg markers, Appendix Table S1) are highlighted in blue.
- F Boxplots showing the distribution of the log normalised expression of *F3* (top) or *Mgp* (bottom) across transcriptomic data of CD142⁻ ASPCs treated with an adipogenic cocktail supplemented with DMSO or different concentrations of RA (0.01–100 μM); the indicated significance is based on the result of differential expression analysis between all RA treated samples or samples treated with RA of a concentration between 0.01 and 1 μM versus controls (treatment with differentiation cocktail with or without DMSO), $n = 2-4$, 2-4 biological replicates, 1 independent well for each.
- G Representative fluorescence microscopy images of CD142⁻ ASPCs, co-cultured with CD142⁺ ASPCs (Aregs; in the top well) subjected to the indicated compounds at the indicated concentrations; AGN and BMS are antagonists of RAR, DEAB is an antagonist of RALDH enzymes which convert retinaldehyde to RA, and HX is an antagonist of RXR.
- H Fraction of differentiated CD142⁻ ASPCs indicated in (G), as quantified by the "adiposcore"; marker shapes correspond to different biological replicates, $n = 4-15$, 2-5 biological replicates, 2-3 independent wells for each.
- I Representative fluorescence microscopy images of CD142⁻ ASPCs, co-cultured with CD142⁺ ASPCs (Aregs) subjected to control (scr) or siRNA-mediated knockdowns of selected RA signalling pathway genes: *Rara*, *Arb*, *Rarg*, *Rbp1* and *Rxrg* after adipogenic differentiation (i.e., after exposure to an adipogenic cocktail, Materials and Methods).
- J Fraction of differentiated CD142⁻ ASPCs indicated in (I), as quantified by the "adiposcore"; marker shapes correspond to different biological replicates, $n = 24-29$, 4 biological replicates, 5-8 independent wells for each.

Data information: In all images, nuclei are stained with Hoechst (blue) and lipids are stained with Bodipy (yellow); scale bars, 100 μm . * $P \leq 0.05$, ** $P \leq 0.01$, *** $P \leq 0.001$, pairwise two-sided t-test (H-J), or one-way ANOVA and Tukey HSD *post hoc* test (A) for statistical details see Materials and Methods.

again rather variable across batches and assays, all the tested antagonists consistently induced a significant decrease in Aregs' capacity to inhibit CD142⁻ ASPC adipogenesis (Fig 5G and H, Appendix Fig S29), an effect that was dose-dependent for AGN, DEAB and HX, while, for the latter, the effect decreased again at the highest HX concentration. Overall, we interpret these observations as being the result of RA pathway interference in Aregs. Indeed, since upon confluency, the permeable transwell membrane is fully covered with cells, we hypothesise that leakage of the antagonist to the bottom well should be minimal. Yet, even if this would nevertheless occur, we observed that the antagonists have a negligible effect on CD142⁻ ASPC differentiation when directly administered to this cell population (Appendix Fig S30). However, the latter observations do not exclude the possibility that the antagonists reduced the ability of CD142⁻ ASPCs to respond to Aregs' paracrine signals by interfering with the RA pathway in these cells. To address this possibility and thus to support the involvement of the RA pathway in Aregs' inhibitory capacity in a more stringent and specific manner, we performed transwell assays in which CD142⁻ ASPCs were co-cultured with CD142⁺ ASPCs in which key genes involved in RA signalling were knocked down using siRNAs (for an assessment of KD efficiency, see Appendix Fig S31C). We focused on *Retinol Binding Protein 1* (*Rbp1*) since it is a top Areg marker (Appendix Fig S23A and Table S1) that has previously been shown to have an anti-adipogenic effect (Zizola et al, 2010). Furthermore, since RA treatment up-regulates the expression of Areg markers, we decided to test different RA-activated nuclear receptors, and specifically *Rara*, *Arb*, *Rarg* given that their expression is enriched in CD142⁺ versus CD142⁻ ASPCs upon exposure to an adipogenic cocktail as well as *Rxrg* which had previously been shown to play a role in adipose biology (Nie et al, 2017). These experiments

revealed that the KD of *Rbp1*, as well as *Rarg* but also *Rxrg* in CD142⁺ ASPCs resulted in increased adipogenesis of co-cultured CD142⁻ ASPCs compared to control CD142⁺ ASPCs (i.e., treated with scrambled siRNA; Fig 5I and J, and Appendix Fig S31).

Together, these findings strongly suggest that the RA signalling pathway plays an important role in mediating the anti-adipogenic capacity of Aregs.

Discussion

In this study, we systematically examined the molecular and phenotypic properties of mouse subcutaneous CD142⁺ ASPCs, motivated by the reported discrepancy regarding their behaviour in the context of adipogenesis (Schwalie et al, 2018; Hwang & Kim, 2019; Merrick et al, 2019; Corvera, 2021; Nguyen et al, 2021; Dong et al, 2022). Using numerous functional and multi-omic assays across distinct experimental settings and sampling conditions, we unambiguously validated the previously proposed non- as well as anti-adipogenic nature of these cells both *in vitro* and *in vivo*, which is why we suggest to retain their initially proposed name: "Aregs" for adipogenesis regulators (Fig 1 and Appendix Figs S1–S10).

These analyses also led to unexpected findings regarding in particular the age-dependent nature of CD142⁺ ASPCs' functional properties. It has been shown that the developmental timing of adipose tissue formation varies largely between species (Carberry et al, 2010; Louveau et al, 2016) and different anatomical fat depots (Birsoy et al, 2011; Han et al, 2011; Rosen & Spiegelman, 2014; Hong et al, 2015). Subcutaneous SVF cells were shown to be capable of differentiating into lipid-filled adipocytes *in vitro* under adipogenic differentiation medium from embryonic day E16.5

(Birsoy *et al*, 2011). However, the dynamics of post-natal ASPC differentiation, as well as the emergence of their cellular heterogeneity, are still poorly understood. Having experimentally investigated diverse murine post-natal developmental stages, we found that all fractions of newborn (P0) ASPCs displayed a molecular identity and behaviour (high proliferative and adipogenic propensity) that resemble those of “naïve preadipocytes” (Appendix Fig S14; Wang *et al*, 2003; Atanassova *et al*, 2012; Hong *et al*, 2015; Hepler & Gupta, 2017). Importantly, P0-derived CD142⁺ ASPCs did not show a higher “Areg/CD142⁺ score” (Appendix Table S1, Appendix Fig S15) nor higher expression of “retinol metabolic process”-related genes (Appendix Fig S14) compared to the other tested ASPC fractions. This is consistent with the notion that all P0 ASPCs are likely still naïve and indicates that the mesenchymal cellular landscape that is observed in adults has not yet been established in newborns. Further inquiry revealed an age-dependent evolution of both the molecular signature and the diverse adipogenic phenotypes of ASPCs. Indeed, we found that the Areg-specific molecular characteristics emerge in CD142⁺ ASPCs before P16, consistent with their detection in P12 scRNA-seq data (Merrick *et al*, 2019) and become most prominent in adulthood (Fig 2A and Appendix Fig S15). Interestingly however, the non- and anti-adipogenic phenotypes of CD142⁺ ASPCs only emerged between post-natal days 16 and 28 (4 wo), thus after the establishment of their molecular identity, with, intriguingly, the weaning of the litters occurring during this time period (Fig 2D and E). We cannot formally point to weaning as the primary causal factor for the observed timing offset between Aregs’ molecular and functional appearance. Yet, the fact that weaning entails a dramatic nutritional alteration makes it an intriguing candidate for further investigation.

While the observed adipogenic phenotype of pre-weaning CD142⁺ ASPCs is rather striking, it still does not fully resolve the reported functional discrepancy for CD142⁺ ASPCs given that an adipogenic propensity has also been reported for adult CD142⁺ APSCs (Merrick *et al*, 2019; Nguyen *et al*, 2021), which contrasts with our results. Recently, Dong *et al* (2022) provided data that are in line with our observed phenotypic properties of CD142⁺ ASPCs. These authors also revealed a functional gradient when sorting cells featuring lower CD142 staining, highlighting that *F3*, while being one of the best markers that characterise Aregs at the transcriptomic level, is not fully specific as it appears also expressed (albeit at lower levels) by a subset of previously characterised highly adipogenic pre-adipocytes (Ferrero *et al*, 2020; Corvera, 2021; Dong *et al*, 2022). This renders the need to uncover how Aregs’ functional properties are molecularly regulated even more pressing, also in light of our findings demonstrating that mouse Aregs can decrease the adipogenic capacity of human subcutaneous adipose tissue-derived SVF cells. Since we demonstrated that Aregs exert their inhibitory properties via paracrine signalling, we focused on genes coding for secreted factors. We identified six candidates that were specific to Aregs across multi-omic datasets: *F3* (coding for CD142) itself, *Mgp*, *Gdf10*, *Clec11a*, *Cpe* and *Bgn*, with CD142 and MGP the most interesting functionally, based on recombinant protein as well as KD assays (Fig 3I and J, Appendix Fig S19, Fig 4A and B). The involvement of CD142 in Aregs’ inhibitory activity is surprising given the reported physiological role of CD142 as a coagulation factor (Chu, 2011). CD142, also known as Tissue factor, is the primary initiator in the extrinsic coagulation pathway (Petersen *et al*, 1995) and has not been explicitly

shown to be involved in adipogenesis-related processes. MGP (Matrix Gla protein, a member of a family of vitamin-K2 dependent, Gla-containing proteins) has been demonstrated to act as an inhibitor of calcification in cartilage and vasculature (Bäck *et al*, 2019), implying its possible specificity to mesenchymal cells with multilineage potential. Finally, while the inhibitory effect of GDF10 has been previously demonstrated in the context of adipogenesis in Areg-like/CD142⁺ muscle-resident stromal cells (Camps *et al*, 2020) as well as in differentiating 3T3-L1 cells (Hino *et al*, 2012), we found that inactivating *Gdf10* in Aregs did not majorly interfere with their inhibitory activity towards other ASPCs.

Next to these secretory proteins, we uncovered the RA-signalling pathway as another likely actor that is involved in the Areg-mediated inhibition of adipogenesis (Fig 5). Retinoic acid has pleiotropic effects, but has long been linked to adipogenic inhibition (Murray & Russell, 1980; Kuri-Harcuch, 1982; Salazarolivo *et al*, 1994; Schwartz *et al*, 1996; Lee *et al*, 2011; Sagara *et al*, 2013; Wang *et al*, 2017) and demonstrated to be protective against diet-induced obesity (Berry & Noy, 2009; Bonet *et al*, 2012). Moreover, the expression of *F3* and *Mgp* has already been shown to be regulated by RA (Balmer & Blomhoff, 2002; Takeda *et al*, 2016), which we also demonstrated for these and other Areg-specific markers (Fig 5F and Appendix Fig S28). This suggests that RA could be an important regulator of Aregs’ phenotype by modulating, among others, the expression of key secretory factors. This hypothesis is consistent with our findings that blocking the physiological production of RA or subsequent activation of nuclear receptors dampened the anti-adipogenic effect of Aregs on CD142⁻ ASPCs (Fig 5G and H, and Appendix Fig S29). We thereby identified three genes involved in the RA signalling pathway, *Rbp1*, *Rxrg* and *Rarg*, as important functional actors in Aregs’ inhibitory capacity (Fig 5I and J). However, given the convoluted nature of RA signalling, further studies will be required to investigate in greater molecular detail how this collection of molecules may precisely cooperate to steer the developmental, phenotypic and functional properties of Aregs, possibly together with other processes such as the Wnt signalling pathway (Appendix Fig S27A), as has been recently reported (Dong *et al*, 2022) and previously shown to cooperate with RA signalling to inhibit adipogenesis (Kim *et al*, 2013).

While we showed that interfering with the RA signalling pathway in Aregs dampens their anti-adipogenic capacity, we cannot exclude that RA might also be involved in impeding CD142⁻ ASPC (i.e., the “receiving cells”) adipogenesis. This notion stems from our observations that Areg-treated CD142⁻ ASPCs exhibited a significantly increased expression of many Areg-specific genes, a number of which were also upregulated in RA-treated CD142⁻ ASPCs (Fig 5F and Appendix Fig S28), rationalising why Areg-treated CD142⁻ ASPCs were found to be transcriptomically more similar to CD142⁻ ASPCs treated with RA than those treated with EGF. These results point to a potential conversion of CD142⁻ ASPCs, when subjected to CD142⁺ ASPC-derived inhibitory signals, into Areg-like cells, consistent with the proposal that various ASPC subpopulations may be able to interconvert within the subcutaneous adipogenic stem cell niche (Merrick *et al*, 2019). Together, our findings suggest that it is, among other possible mechanisms, the RA-induced expression of Areg markers in CD142⁻ ASPCs that impedes differentiation of the latter cells. Interestingly, many Areg markers were reported to be higher expressed in visceral compared to subcutaneous ASPCs and

have as such been associated with the impaired capacity of visceral ASPCs to give rise to *in vitro* adipocytes (Reichert *et al*, 2011; Meissburger *et al*, 2016; Takeda *et al*, 2016; Ferrero *et al*, 2020; Li *et al*, 2020). This further supports the hypothesis that RA signalling may well be operational in both Aregs and CD142⁻ ASPCs, suggesting a complex molecular interplay of pro- and anti-adipogenic signals among ASPCs, whose underlying mechanisms and functional relevance in adipose tissue development and homeostasis warrants further investigation.

Materials and Methods

Bioethics

All mouse experiments were conducted in strict accordance with the Swiss law and all experiments were approved by the ethics commission of the state veterinary office (VD2984/20, VD3406/2018, VD3406x1/2022, VD3474/2019).

All human material used in this study has been obtained from donors of two independent cohorts: the Cohort of Obese Patients of Lausanne using an ethically approved licence by the commission of the Vaud Canton (CER-VD Project PB_2018–00119) and a control healthy cohort from renal transplantation donors using an ethically approved licence by the commission of the Vaud Canton (CER-VD 2020–02021). The coded samples were collected under signed informed consent conforming to the guidelines of the 2000 Helsinki declaration. For information on sex, age and BMI of human participants, see Appendix Table S3.

Animals

C57BL/6J WT (C57BL/6NCrl – Strain number: 026), CD1 WT (Crl: CD1 – Strain number: 022) and Ob/Ob (B6.Cg-Lepob/J – Strain number: 606) mice were obtained from Charles River Laboratories and 129SVE (129S6/SvEvTac) mice were obtained from Taconic.

Analysis and integration of single-cell datasets

Integration of adult mouse subcutaneous adipose tissue

The integration of the three datasets of adult mouse subcutaneous adipose tissue published by Burl *et al* (2018), Merrick *et al* (2019) and Schwalie *et al* (2018) was performed as described in Ferrero *et al* (2020). The clustering tree plot was generated using the function `clustree()` from the package *clustree* version 0.4.3. (Zappia & Oshlack, 2018).

Analysis and integration of P12 mouse subcutaneous adipose tissue

The scRNA-seq count matrices from Merrick *et al* (2019) (GSM3717977) were downloaded from the Gene Expression Omnibus (GEO) repository. The datasets were first analysed separately to identify the main clusters as described in Ferrero *et al* (2020). Differential expression analysis between the different clusters was performed using the function `FindAllMarkers()` from *Seurat* (Hao *et al*, 2021), only the markers detected as significant (FDR < 0.05 and logFC > 0.25, as defined by default) by both Wilcoxon Rank Sum test (test.use = “wilcox”) and Likelihood-ratio test

for single cell gene expression (test.use = “bimod”) were selected. This dataset was then integrated with the three adult datasets discussed above following similar methods as the one described in Ferrero *et al* (2020). The “CD142⁺ score” was calculated using the function `AddModuleScore()` of *Seurat* (Hao *et al*, 2021) giving as features the top CD142⁺ markers (see “Selection of CD142⁺ top 100 markers”; Fig 2A and Appendix Fig S11E).

Comparison of male and female ASPCs

The single-cell RNA-seq dataset published in Schwalie *et al* (2018) (<https://www.ebi.ac.uk/arrayexpress/experiments/E-MTAB-6677>) contains both male and female cells. A strict filtering based on the expression of Y-chromosome genes (*Ddx3y*, *Eif2s3y*, *Kdm5d*, *Uty* and *Sult1e1*) and the local minimum of *Xist* expression was used to separate male and female cells. More precisely, female cells were defined as cells expressing *Xist* above the defined threshold and not expressing any of the Y-chromosome genes, and male cells were defined as cells expressing at least one of the Y-chromosome genes and not *Xist*. The other cells were filtered out. The two groups, female and male cells, were analysed separately. For each, genes not expressed in at least three cells, were filtered out. The data were log normalised using the functions `ComputeSumFactor()` to which the results of the function `quickCluster()` was given as input to the parameter `clusters`, and the function `normalise()` from the package *SCRAN M3Drop* (Andrews & Hemberg, 2019) was used to find the highly variable genes. A *Seurat* object was created, the data were scaled for the number of features and number of UMIs. The PCA was computed, and the first × significant PCs defined by the JackStraw test implemented in *Seurat* (Hao *et al*, 2021) were used to build the tSNE. Clustering was performed using the function `sc3()` from the package *SC3* (Kiselev *et al*, 2017). Differential expression analysis between the different clusters was performed using the function `FindAllMarkers()` from *Seurat* (Hao *et al*, 2021), only the markers detected as significant (FDR < 0.05 and logFC > 0.25, as defined by default) by both the Wilcoxon Rank Sum test (test.use = “wilcox”) and Likelihood-ratio test for single-cell gene expression (test.use = “bimod”) were selected. The top differentially expressed genes of males were ranked by logFC and the top 100 were used to generate Appendix Fig S9B.

Comparison of top markers between scRNA-seq results

Appendix Fig S9B displays the percentage of the top 100 markers shared between the different displayed populations. The male markers were identified using differential expression analysis as described in “Comparison of male and female ASPCs”. For the left barplot, the male markers were compared to the top 100 markers published in Schwalie *et al* (2018) as Appendix Table S2. For the right bar plot, the male markers were compared to the top 100 markers identified for the three main ASPCs population based on the integration analysis that we performed as described in “Integration of adult mouse subcutaneous adipose tissue”. Appendix Fig S11A shows the percentage of the top 60 markers identified of the three main subpopulations of ASPCs in P12 as described in “Analysis and integration of p12 mouse subcutaneous adipose tissue”, compared to the top 60 adult markers (ranked by logFC) of the same subpopulations identified based on the integration analysis that we performed described in “Integration of adult mouse subcutaneous adipose tissue”. For this figure, only the top 60

markers were used as one of the populations of the P12 datasets did not have more than 60 markers that were defined as differentially expressed based on our filtering, which is not uncommon in scRNA-seq analysis

Selection of CD142⁺ top 100 markers

Three single-cell RNA-seq datasets of subcutaneous murine fat tissues from Schwalie *et al*, Merrick *et al* and Burl *et al* were integrated using the Seurat pipeline (Hao *et al*, 2021) as described in the supplementary Methods of Ferrero *et al* (2020). The differentially expressed genes of the Areg (*F3*⁺) cluster were the genes identified as differentially expressed in all three batches and with a corrected *P*-value below 0.05. More precisely, the cells of the Areg (*F3*⁺) cluster of the integration were sorted by batch. Within their respective dataset, DE genes were identified using the FindMarkers() function of Seurat (Hao *et al*, 2021) with the Wilcoxon Rank Sum test (logfc.threshold = 0.25, min.pct = 0.1). Only genes identified as differentially expressed in all the batches and with a positive log fold change were considered. The *P*-values were corrected using the Fisher() function from the metaseqR package. Eighty-five genes of this list had an adjusted *P*-value < 0.05. The top 20 differentially expressed genes in CD142⁺ versus CD142⁻ ASPCs bulk RNA-seq published in Schwalie *et al* were added to yield a final list of 100 top markers, referred to as “Top CD142⁺ markers”, as well as “Areg markers” in the manuscript (Appendix Table S1).

Isolation of the mouse stromal vascular fraction (SVF)

Subcutaneous adipose tissue depots were dissected from wild-type C57BL/6J male and female mice of different ages P12–17 (12–17 days post-birth), 4-, 7- and 11-week-old into PBS. The tissue was subsequently minced using scissors, transferred into collagenase (Sigma-Aldrich #C6885-1G, 2 mg/ml of homemade collagenase buffer (25 mM of NaHCO₃, 12 mM of KH₂PO₄, 1.2 mM of MgSO₄, 4.8 mM of KCl, 120 mM of NaCl, 1.4 M of CaCl₂, 5 mM of Glucose, 2.5% BSA, pH = 7.4)), incubated for 65–70 min at 37°C under agitation (130 rpm on a vertical shaker) and resuspended after 45–50 min of digestion. The cell suspension was then diluted with PBS (with the aim of diluting the collagenase and stopping/slowing down the digestion) filtered through a 100-µm, then 40-µm cell strainer in order to ensure a single cell suspension. Next, the cells were pelleted by a 5 min centrifugation at 400 g at room temperature and red blood cells were lysed by incubating the pellet with a homemade red blood cell lysis buffer (154 mM NH₄Cl, 10 mM KHCO₃, 0.1 mM EDTA) for a maximum of 5 min, followed by two washes (a 5 min centrifugation at 400 g, room temperature) with a homemade FACS buffer (PBS with 3% foetal bovine serum (FBS; Gibco #10270–106), 1 mM EDTA, 1% penicillin–streptomycin (Gibco #15140122)).

Isolation of SVF cells from new-born mice

Burgeoning depots of inguinal subcutaneous adipose tissue were dissected from new-born (NB) wild-type C57BL/6J mice into PBS. The tissue was transferred into collagenase solution (see above) and incubated for 1 h at 37°C under agitation (130 rpm on a vertical shaker) and resuspended after 45 min of digestion. The cell

suspension was then filtered through a 100-µm, then 40-µm cell strainer in order to ensure a single cell preparation. Next, the cells were pelleted by a 5-min centrifugation at 400 g at room temperature and a red blood cell lysis was performed by incubating the pellet in a homemade red blood cell lysis buffer (see above) for 5 min, followed by two washes (a 5-min centrifugation at 400 g, room temperature) with a homemade FACS buffer (see above).

FACS-based cell isolation of mouse ASPCs

The SVF cell suspension was diluted to 1×10^7 cells/ml with a homemade FACS buffer (see above) and the following fluorophore-conjugated antibodies were added (in titration-determined quantities, Appendix Table S4): anti-mouse CD31–AF488, anti-mouse CD45–AF488, anti-mouse TER119–AF488 (BioLegend #303110, #304017 and #116215, respectively) for selecting the Lin⁻ population; anti-mouse SCA1-PE-Cy7 (BioLegend #122513) to enrich the Lin⁻ population with ASPCs; and four different anti-mouse CD142 antibodies: (i) anti-mouse CD142 SinoBiological (SB), monoclonal rabbit IgG clone #001, PE-conjugated, #50413-R001-PE, (ii) SinoBiological, monoclonal rabbit IgG clone #001, #50413-R001, in-house conjugated to Lightning-Link PE with Conjugation Kit (Innova Biosciences #703–0010) (SB-LL), (iii) BiOrbyt, monoclonal mouse IgG clone HTF-1, PE-conjugated, # ORB507485 (BO) and (iv) R&D Systems, polyclonal goat IgG, PE-conjugated, #FAB3178P (R&D). The cells were incubated with the antibodies on ice for at least 30 min and protected from light, after which they were washed with the FACS buffer, stained with propidium iodide (Molecular Probes #P3566) for assessing viability, filtered through a 40-µm cell strainer and subjected to FACS with the use of a Becton Dickinson FACS Aria II sorter. Compensation measurements were performed for single stains using positive/negative compensation beads (eBiosciences #01-2222-42).

The following gating strategy was applied while sorting the cells: first, the cells were selected based on their size and granularity/complexity (side and forward scatter), followed by a double elimination of any events that could represent more than one cell. Next, the Lin⁻ (CD31⁻ CD45⁻ TER119⁻) population was selected, followed by a Lin⁻ SCA1⁺ selection (ASPCs), and finally, ASPC cells that were negative or positive for CD142 marker: Lin⁻SCA1⁺ CD142⁻ (CD142⁻ ASPCs) and Lin⁻SCA1⁺ CD142⁺ (CD142⁺ ASPCs, Aregs). The measurements were acquired using Diva software supplemented on the Becton Dickinson FACS Aria II sorter and analysed using FlowJo analysis software.

In vitro adipogenic differentiation of mouse ASPCs

Equal cell numbers were sorted or plated in flat-bottom microscopy-adapted cell culture plates (Corning #353219), cultured in high glucose DMEM medium (Gibco #61965026) supplemented with 10% FBS and 1% penicillin–streptomycin, and treated with a single dose of white adipocyte differentiation induction cocktail at confluence (0.5 µM 3-isobutyl-1-methylxanthine (IBMX, Sigma #15879), 1 µM dexamethasone (Sigma #D2915), 170 nM (1 µg/ml) insulin (Sigma #19278)), followed by a maintenance treatment 2–3 days post-induction (170 nM insulin) and refreshed every 2–3 days. The culture was carried out until days 6–8 after induction, at which point cells were stained for imaging or collected for RNA extraction.

In vitro adipogenic differentiation of mouse ASPCs using various differentiation cocktails

Equal cell numbers were sorted or plated as described above. At confluence, the cells were treated with a single dose of one of four different versions of white adipocyte differentiation induction cocktails: (i) the classical complete cocktail in DMEM medium: 0.5 μ M IBMX, 1 μ M dexamethasone, 170 nM (1 μ g/ml) insulin; (ii) minimal cocktail in DMEM medium: 170 nM insulin; (iii) Complete cocktail + Indomethacin + T3 in DMEM/F12 (1:1 ratio) medium: 0.5 μ M IBMX, 1 μ M dexamethasone and 20 nM insulin, 125 nM indomethacin, 1 nM Triiodothyronine (T3); and (iv) Minimal cocktail in DMEM/F12 medium: 20 nM insulin. After 2–3 days of induction, maintenance cocktail was applied every 2–3 days with (i) 170 nM insulin in DMEM for cocktail 1; (ii) DMEM for cocktail 2; (iii) 20 nM insulin in DMEM/F12 for cocktail 3; (iv) DMEM/F12 for cocktail 4. DMEM for all the corresponding treatments was supplemented with 10% FBS and 1% penicillin–streptomycin. DMEM/F12 for all the corresponding treatments was supplemented with 10% FBS and 50 ng/ml Primocin. The culture was carried until day 6–8 post induction.

Imaging and quantification of *in vitro* adipogenesis

Once the cells differentiated fully, they were stained with live fluorescence dyes: Bodipy (boron-dipyrromethene, Invitrogen #D3922) for lipids and Hoechst for nuclei. Cells were incubated with the dyes in FluoroBrite, phenol red-free DMEM medium (Gibco #A1896701), supplemented with 10% FBS and 1% penicillin–streptomycin for 30 min at 37°C in the dark, washed twice with PBS and imaged in FluoroBrite medium. Given a substantial variation in the extent of lipid accumulation by the tested cell fractions (within the same well but also across the technical replicates), the imaging was optimised to cover the largest surface of the well possible. Moreover, a z-stack acquisition in a spinning-disc mode and Z-projection were performed in order to capture the extent of *in vitro* adipogenesis with the highest possible accuracy (Appendix Fig S32). Specifically, the automated platform Operetta (Perkin Elmer) was used for imaging. First, 7–8 z-stacks were acquired for every field of view (Appendix Fig S32A) in a confocal-mode of the microscope in order to produce high quality images for downstream z-projection and accurate thresholding (Appendix Fig S32B). Next, 25 images per well were acquired (Appendix Fig S32C) using a Plan Neofluar 10 \times Air, NA 0.35 objective, with 10% overlap for further tiling and with the aim of covering the majority of the well for accurate representation of lipid accumulation (Appendix Fig S32D). For experiments in Figs 3A and F, 4A, 5G and I, Appendix Figs S17, S21A, C and H, S29A and S31A, 12 images per well were acquired using a Plan Apochromat 10 \times Air, NA 0.8 objective, with 10% given a different cell culture plate used (see “Transwell experiments”). The Hoechst, blue channel was acquired with 40 ms exposure time and 50% of the illumination power while the Bodipy, green channel was acquired with 20 ms exposure time and 50% of the illumination power. The images, supported by Harmony software, were exported as TIFF files. They were subsequently tiled using the acquired 10% image overlap and Z-projection was performed with the maximum intensity of acquired z-stacks. To accurately estimate and represent

differences in adipocyte differentiation, a quantification algorithm for image treatment was developed in collaboration with the EPFL BIOP imaging facility. In brief, image analysis was performed in ImageJ/Fiji, lipid droplets (yellow) and nuclei (blue) images were filtered using a Gaussian blur (sigma equal to 2 and 3, respectively) before an automatic thresholding. The automatic thresholding algorithm selections were chosen based on visual inspection of output images. The areas corresponding to the thresholded lipid and nuclei signals were next used to calculate the normalised lipid accumulation (Adiposcore) and to finally score the assessed individuals based on the degree of adipocyte differentiation potential *in vitro*.

In the main figures, representative blown-up crop images of each sample are shown. In supplementary figures, tiled (25 images) and thresholded (both lipid – yellow and nuclei – blue channels) images are shown. Plotted ratios were normalised to the indicated control in all figures except Fig 2E and the corresponding Appendix Fig S12D, where non-normalised values from 13 independent experiments were plotted together, hence the variation is more substantial.

***In vivo* characterisation of Aregs and adipocyte formation quantification**

Subcutaneous injections of 150 μ l of Matrigel (Corning #356234) containing either 100% CD142[−] ASPCs versus 80–90% CD142[−] ASPCs mixed with 10–20% Aregs were performed. After 3 weeks of high-fat diet feeding of the respective C57BL/6J mice, all Matrigel plugs were excised and fixed in 4% paraformaldehyde (PFA) overnight, dehydrated and embedded in paraffin. Sections of 4 μ m were stained with haematoxylin and eosin. From each plug, images of at least three full sections were taken and adipocyte numbers were quantified using a new method of quantification allowing assessment of both the number and size of adipocytes in a reliable fashion, as described in detail in Tratwal *et al* (2020) (Fig 3C and D).

Mass spectrometry sample preparation of mouse ASPCs

FACS-sorted cells were vacuum-centrifuged to near dryness and resuspended in 9 μ l of 100 mM HEPES pH 8, 10 mM tris(2-carboxyethyl)phosphine. Samples were first heated for 20 min at 95°C with permanent shaking and then sonicated in a water bath for 15 min. Extracted proteins were alkylated with 1 μ l of 400 mM chloroacetamide for 30 min at 37°C in the dark with permanent shaking. Proteins were digested overnight using 200 ng mass spectrometry grade trypsin with permanent shaking. Resulting peptides were desalted on C18 StageTips (Rappsilber *et al*, 2007) and dried by vacuum centrifugation. For TMT labelling, peptides were first reconstituted in 8 μ l HEPES 100 mM pH 8 and 3 μ l of TMT solution (20 μ g/ μ l in pure acetonitrile) were then added. Labelling was performed at room temperature for 1.5 h and reactions were quenched with hydroxylamine to a final concentration of 0.4% (v/v) for 15 min. TMT-labelled samples were then pooled at a 1:1 ratio across all samples. A single shot control LC–MS run was performed to ensure similar peptide mixing across each TMT channel to avoid the need of further excessive normalisation. Quantities of each TMT-labelled sample were adjusted according to control run. The combined sample was vacuum-centrifuged and fractionated into eight

fractions using the Pierce High pH Reversed-Phase Peptide Fractionation Kit following the manufacturer's instructions. Resulting fractions were dried by vacuum centrifugation and again desalted on C18 StageTips.

Each individual fraction was then resuspended in 2% acetonitrile, 0.1% FA and nano-flow separations were performed on a Dionex Ultimate 3000 RSLC nano UPLC system on-line connected with a Lumos Fusion Orbitrap Mass Spectrometer. A capillary pre-column (Acclaim Pepmap C18, 3 μm -100 \AA , 2 cm \times 75 μm ID) was used for sample trapping and cleaning. Analytical separations were performed at 250 nl/min over 150 min biphasic gradients on a 50 cm long in-house packed capillary column (75 μm ID, ReproSil-Pur C18-AQ 1.9 μm silica beads, Dr. Maisch). Acquisitions were performed through Top Speed Data-Dependent acquisition mode using a 3-s cycle time. First MS scans were acquired at a resolution of 120,000 (at 200 m/z) and the most intense parent ions were selected and fragmented by High energy Collision Dissociation (HCD) with a Normalised Collision Energy (NCE) of 37.5% using an isolation window of 0.7 m/z. Fragmented ions scans were acquired with a resolution 50,000 (at 200 m/z) and selected ions were then excluded for the following 120 s.

Mass spectrometry data analysis

Raw data were processed using SEQUEST, Mascot, MS Amanda (Dorfer *et al*, 2014) and MS Fragger (Kong *et al*, 2017) in Proteome Discoverer v.2.4 against the Uniprot Mouse Reference Proteome (Uniprot Release: 2020_05). Enzyme specificity was set to Trypsin and a minimum of six amino acids was required for peptide identification. Up to two missed cleavages were allowed and a 1% FDR cut-off was applied both at peptide and protein identification levels. For the database search, carbamidomethylation (C) and TMT tags (K and Peptide N termini) were set as fixed modifications whereas oxidation (M) was considered as a variable one. The resulting text files were processed through in-house written R scripts (version 3.6.3). Two steps of normalisation were applied. The first step of normalisation was the sample loading normalisation (Plubell *et al*, 2017). Assuming that the total protein abundances were equal across the TMT channels, the reporter ion intensities of all spectra were summed, and each channel was scaled according to this sum, so that the sum of reporter ion signals per channel equals the average of the signals across samples. Then the Trimmed M-Mean normalisation step was also applied using the package EdgeR (Robinson *et al*, 2010; version 3.26.8). Assuming that the samples contain a majority of non-differentially expressed proteins, this second step calculates normalisation factors according to these presumed unchanged protein abundancies. Proteins with high or low abundances and proteins with larger or smaller fold-changes were not considered. Differential protein expression analysis was performed using the R bioconductor package limma (version 3.34.9, 2018-02-22; Ritchie *et al*, 2015), followed by the Benjamini-Hochberg multiple-testing method (Benjamini & Hochberg, 1995). Adjusted *P* values lower than 0.05 (FDR < 0.05) and absolute log₂ fold-change > 1 were considered as significant.

GSEA enrichment analysis (Appendix Fig S23C) was performed using the gseGO() function on the proteins ranked by the logFC of the protein expression in freshly isolated CD142⁺ versus CD142⁻ ASPCs.

In vitro adipogenic differentiation of mouse ASPCs exposed to recombinant proteins and retinoic acid

Equal cell numbers were sorted or plated in flat-bottom microscopy-adapted cell culture plates and cultured as described above. At confluence, the cells were treated with a single dose of classical white adipocyte differentiation induction cocktail at half of its usual concentration: 0.25 μM IBMX, 0.5 μM dexamethasone, 85 nM (0.5 $\mu\text{g}/\text{ml}$) insulin (in DMEM supplemented with 10% FBS and 1% penicillin-streptomycin), supplemented with the following recombinant proteins: BSA (Sigma, # A3059, A9418), EGF (ThermoFisher Scientific, # PMG8043), CD142 (LifeSpan BioSciences, # LS-G12283), MGP (LifeSpan BioSciences, #LS-G13865), CLEC11A (R&D Systems, #3729-SC), GDF10 (SinoBiological, #50165-M01H), CPE (ArcoBioSystems, #CAE-M5222) and BGN (R&D Systems, #8128-CM) at various concentrations including all or some of: 10, 50, 100, 500, 750 and 1,000 ng/ml. For retinoic acid treatments, the above-described differentiation and maintenance cocktails were supplemented with retinoic acid (Sigma, # R2625) diluted in Dimethyl sulfoxide (DMSO, AppliChem, #A36720250). The corresponding doses of the recombinant proteins and the retinoic acid were applied after 2–3 days of induction with the maintenance medium at half of its usual concentration, 85 nM (0.5 $\mu\text{g}/\text{ml}$) insulin in DMEM supplemented with 10% FBS and 1% penicillin-streptomycin.

In vitro adipogenic differentiation of mouse ASPCs exposed to antagonists and inhibitors of the retinoic acid pathway

Equal cell numbers were sorted or plated in flat-bottom microscopy-adapted cell culture plates and cultured as described above. At confluence, the cells were treated with a single dose of classical white adipocyte differentiation induction cocktail at half of its usual concentration: 0.25 μM IBMX, 0.5 μM dexamethasone, 85 nM (0.5 $\mu\text{g}/\text{ml}$) insulin (in DMEM supplemented with 10% FBS and 1% penicillin-streptomycin), supplemented with the inverse RAR agonist BMS493 (referred as BMS in the manuscript; Sigma, #B6688) at concentrations of 100, 200 and 500 nm/ml, the RAR antagonist AGN 193109 (referred as AGN in the manuscript; Sigma, #SML2034), the inhibitor of RALDH1, DEAB (4-Diethylaminobenzaldehyde; Fisher, #11419423) and the RXR antagonist HX531 (referred as HX in the manuscript; Sigma, #SML2170), all three at concentrations of 1, 5 and 10 nm/ml (Fig 5G and H, and Appendix Fig S29). The corresponding doses of the compounds were applied after 2–3 days of induction with the maintenance medium at half of its usual concentration, 85 nM (0.5 $\mu\text{g}/\text{ml}$) insulin in DMEM supplemented with 10% FBS and 1% penicillin-streptomycin.

siRNA-mediated knockdown experiments

For each gene, a pool of three siRNA probes (IDT, TriFECTA DsiRNAs, Appendix Table S5) was reverse-transfected to CD142⁺ ASPCs (Aregs) or ASPCs. Seventy-five thousand cells/cm² were plated in siRNA mix containing 20 nM of each siRNA re-suspended in 1.5% Lipofectamine RNAiMAX (Invitrogen #13778150) that was dissolved in Opti-MEM I reduced serum medium (Invitrogen #31985062), and high glucose DMEM medium supplemented with 2.5% FBS (w/o penicillin-streptomycin). After 24 h, the medium

was changed to high glucose DMEM medium supplemented with 10% FBS and 1% penicillin–streptomycin and after 48 h, the cells were collected for determining overall knockdown efficiency (see “RNA isolation and quantitative PCR”) or induced with white adipogenic differentiation cocktail (see “*In vitro adipogenic differentiation*”).

Transwell experiments

Wild-type Aregs or Aregs subjected to the indicated gene knockdowns (knockdowns performed in the transwell, see “siRNA-mediated knockdown experiments”) were plated in the transwell inserts (Corning #3381). Twenty-four hours after transfection, the cells in inserts were washed with PBS and changed to high glucose DMEM medium supplemented with 10% FBS and 1% penicillin–streptomycin. Forty-eight hours post-transfection, the inserts were placed above previously plated CD142⁻ ASPC cells (cultured in transwell-receiving cell culture plates (Corning #3382)) and both cell populations were treated with white adipocyte differentiation cocktail (see “*In vitro adipogenic differentiation*”) and imaged at days 6–8 after induction (see “Imaging and quantification of *in vitro adipogenesis*”; Figs 4A, and 5I and J, Appendix Figs S2I and S3I).

Aregs were plated in the transwell inserts (Corning #3381), and at confluency, they were treated with the above-mentioned retinoic acid pathway interfering compounds and the inserts were placed above previously plated CD142⁻ ASPC cells (cultured in the transwell-receiving cell culture plates (Corning #3382)) and both cell populations were treated with white adipocyte differentiation cocktail (see “*In vitro adipogenic differentiation*”) and imaged at days 6–8 after induction (see “Imaging and quantification of *in vitro adipogenesis*”; Fig 5G, Appendix Fig S29).

Isolation of the human stromal vascular fraction (SVF)

Subcutaneous adipose tissue biopsies were washed in PBS to remove excess blood, weighed and finely minced using scissors. Minced adipose tissue was incubated with 0.28 U/ml of liberase TM (Roche #05401119001) in DPBS with calcium and magnesium (Gibco #14040091) for 60 min at 37°C under agitation (130 rpm on a vertical shaker). A vigorous shaking was performed after 45 min of incubation to increase the yield of recovered SVF cells. The digested tissue was mixed with equal volume of 1% human albumin (CSL Behring) in DPBS^{-/-} (Gibco #14190094) to stop the lysis. Following a 5-min centrifugation at 400 g at room temperature, floating lipids and mature adipocytes were discarded by aspiration and the cell suspension was filtered through sequential 100- μ m and 40- μ m cell strainers to ensure a single cell preparation. To lyse red blood cells, pelleted SVF was resuspended in VersaLyse solution (Beckman Coulter #A09777) according to the manufacturer’s recommendations and washed once with 1% albumin solution. Such obtained red blood cell-free SVF suspension was plated at a density of at least 100,000 SVF cells per square centimetre in high glucose MEMalpha medium (Gibco #32561037) supplemented with 5% human platelet lysate (Sigma #SCM152) and 50 μ g/ml Primocin (InvivoGen #ant-pm-2). For expanded human ASPCs, TrypLE Select reagent (Gibco #12563011) was used to collect the cells from the cell culture plates.

Differentiation of human subcutaneous stromal vascular fraction (SVF)

The cells at confluence were treated with induction cocktail (high glucose DMEM (#61965), 10% FBS, 50 μ g/ml Primocin, 0.5 mM IBMX (Sigma #15879), 1 μ M dexamethasone (Sigma #D2915), 1.7 μ M insulin (Sigma #19278), 0.2 mM indomethacin (Sigma #I7378) for 7 days), followed by maintenance cocktail treatment (high glucose DMEM, 10% FBS, 50 μ g/ml Primocin, 1.7 μ M insulin) for another 7 days.

RNA isolation and quantitative PCR

Cells subjected to siRNA-mediated knockdowns were collected into Tri-Reagent (Molecular Research Center #TR118) 48 h post-transfection. The direct-zol RNA kit (Zymo Research #R2052) was used to extract RNA, followed by reverse transcription using the SuperScript VILO cDNA Synthesis Kit (Invitrogen). Expression levels of mRNA were assessed by real-time PCR using the PowerUp SYBR Green Master Mix (Thermo Fisher Scientific #A25743). mRNA expression was normalised to the *Hprt1* gene.

Bulk RNA-seq

Barcoded mRNA bulk sequencing (BRB-seq) was performed as previously described (Alpern *et al.*, 2019) and further detailed by the Mercurius™ Protocol by Alithea Genomics. In brief, 7–200 ng of total RNA from each sample were reverse-transcribed in a 96-well plate using SuperScript™ II Reverse Transcriptase (Lifetech 18064014) with individual barcoded oligo-dT primers, featuring a 12-nt-long sample barcode (IDT). Double-stranded cDNA was generated by the second strand synthesis via the nick translation method. For that, a mix containing 2 μ l of RNase H (NEB, #M0297S), 1 μ l of *Escherichia coli* DNA ligase (NEB, #M0205 L), 5 μ l of *E. coli* DNA Polymerase (NEB, #M0209 L), 1 μ l of dNTP (10 mM), 10 μ l of 5 \times Second Strand Buffer (100 mM of Tris, pH 6.9), (AppliChem, #A3452); 25 mM of MgCl₂ (Sigma, #M2670); 450 mM of KCl (AppliChem, #A2939); 0.8 mM of β -NAD (Sigma, N1511); 60 mM of (NH₄)₂SO₄ (Fisher Scientific Acros, #AC20587); and 11 μ l of water were added to 20 μ l of ExoI-treated first-strand reaction on ice. The reaction was incubated at 16°C for 2.5 h. Full-length double-stranded cDNA was purified with 30 μ l (0.6 \times) of AMPure XP magnetic beads (Beckman Coulter, #A63881) and eluted in 20 μ l of water.

The Illumina-compatible libraries were prepared by tagmentation of 10–40 ng of full-length double-stranded cDNA with 1 μ l of in-house produced Tn5 enzyme (11 μ M). After tagmentation, the libraries were purified with DNA Clean and Concentrator kit (Zymo Research #D4014) eluted in 20 μ l of water and PCR amplified using 25 μ l NEB Next High-Fidelity 2 \times PCR Master Mix (NEB, #M0541 L), 2.5 μ l of each i5 and i7 Illumina index adapter (IDT) using the following program: incubation 72°C—3 min, denaturation 98°C—30 s; 15 cycles: 98°C—10 s, 63°C—30 s, 72°C—30 s; final elongation at 72°C—5 min. The libraries were purified twice with AMPure beads (Beckman Coulter, #A63881) at a 0.6 \times ratio to remove the fragments < 300 nt. The resulting libraries were profiled using a High Sensitivity NGS Fragment Analysis Kit (Advanced Analytical, #DNF-474) and measured using a Qubit dsDNA HS Assay Kit

(Invitrogen, #Q32851) prior to pooling and sequencing using the Illumina NextSeq 500 platform using a custom primer and the High Output v2 kit (75 cycles; Illumina, #FC-404-2005). The library loading concentration was 2.4 pM and sequencing configuration was as follows: R1 21c/index i7 8c/index i5 8 c/R2 55c.

Analysis of bulk RNA-seq

Preprocessing

After sequencing and standard Illumina library demultiplexing, the *.fastq* files were aligned to the mouse reference genome mm10 (GRCm38 release 100 from Ensembl) using STAR (Version 2.7.3a), excluding multiple mapped reads. Resulting BAM files were sample-demultiplexed using BRB-seqTools v.1.4 (<https://github.com/DeplanckeLab/BRB-seqTools>) and the “gene expression × samples” read and UMI count matrices were generated using HTSeq v0.12.4.

General methods

Samples with a too low number of reads or UMIs were filtered out. Genes with a count per million greater than 1 in at least three samples were retained. Raw counts were then normalised as log counts per millions with a pseudo count of 1, using the function `cpm()` from *EdgeR* (McCarthy et al, 2012) version 3.30.3. If the samples were from different batches, the raw counts were first normalised using quantile normalisation as implemented in `voom()` from the package *limma* (Ritchie et al, 2015) version 3.44.3 and then corrected for batch effects using `combat()` from *sva* version 3.36.0. PCAs were computed using `prcomp` with the parameters `centre` and `scale set` to `TRUE`.

Differential expression analyses were performed using *DESeq2* (Love et al, 2014) version 1.28.1 and adding `batch` as a cofactor if necessary.

Scores

Scores were calculated as the sum of the normalised expression scaled between 0 and 1 per gene of gene lists defined as followed:

- i “CD142⁺ score” was based on the top CD142⁺ markers (Appendix Table S1), defined in “Selection of Areg top 100 markers” (Fig 1G, Appendix Fig S10E, Fig 2G and H, Appendix Fig S11E, Figs 4F and 5D).
- ii “White fat cell differentiation score” was based on the genes of the GO term GO:0050872 (Figs 1H, and 4F and G, Appendix Fig S22A, B and E, Fig 5D).
- iii “Negative regulation of fat cell differentiation score” was based on the genes of the GO term GO:0045599 (Fig 1I).
- iv “Retinol metabolic process score” was based on the genes of the GO term GO:0042572 (Appendix Fig S14C).
- v “Retinoic acid score” (RAS) was based on the genes of the GO terms “Cellular response to RA” (GO:0071300) and “RA receptor signalling pathway” (GO:0048384) (Fig 5D and E).

Gene expression heatmaps

Heatmaps of Figs 1C, 3E and D, 4D, and 5B and C, Appendix Figs S4A, S24A, S27B and S28A display row-normalised expression and were generated using *pheatmap* version 1.0.12. The columns and rows were clustered using the method “ward.2D” of `hclust()` of the package *stats*.

Gene set enrichment analysis

Gene set enrichment analysis was performed using the package *clusterProfiler* (Yu et al, 2012) version 3.16.1.

- i Appendix Figs S6B, S22A, and S23D and E: GSEA was performed using the `gseGO()` function on the genes ranked by the Wald statistic computed by differential expression analysis of CD142⁺ versus CD142⁻ ASPCs post-differentiation.
- ii Appendix Figs S13A, S14A and B: GSEA was performed using `gseGO()` on the genes ranked by their loadings along the first principal component (PC1) of the PCA of freshly sorted total, CD142⁺ and CD142⁻ ASPCs at different ages (Fig 2F), showing that samples are ordered by age along PC1.
- iii Appendix Fig S15A: GSEA was performed on the same ranking as Appendix Fig S13A described just above using `GSEA()` inputting the top CD142⁺ markers (Appendix Table S1), as tested gene set.
- iv Appendix Fig S15B–E: GSEA was performed on the genes ranked by the Wald statistic computed by the differential expression analysis of freshly sorted CD142⁺ versus CD142⁻ ASPCs performed by age (P0, P16, 4 wo and adult (7 and 11 wo)). The top 100 CD142⁺ markers (Appendix Table S1) were given as input gene set to `GSEA()`.
- v Fig 5B, Appendix Fig S23B: GSEA was performed using the `gseGO()` function on the genes ranked by the Wald statistic computed by the differential expression analysis of freshly sorted CD142⁺ versus CD142⁻ ASPCs.
- vi Appendix Fig S22C, and S24B and C: GSEA was performed on the genes ranked by their loadings along PC1 of the PCA display in Fig 4C using `GSEA()` testing for the three gene sets: top CD142⁺ markers, GO:0071300 “Cellular response to RA” and GO:0048384 “RA receptor signalling pathway”. Significant positive enrichment was also obtained when GSEA was performed on the Wald statistic computed by the differential expression analysis of CD142⁻ ASPCs co-cultured with active Aregs (si*Gdf10*, scr, WT) and CD142⁺ ASPCs post-differentiation versus CD142⁻ ASPCs co-cultured with dysfunctional Aregs (si*F3*, si*Mgp*) or CD142⁻ ASPCs alone post-differentiation. Significant negative enrichment was also obtained when GSEA was performed on the genes ranked by the coefficient of the linear regression performed between “White fat cell differentiation score” and gene expression of the same dataset (see “Additional analyses specific to CD142⁻ ASPCs co-cultured with KD Aregs” for further details).

Additional analyses specific to age samples

Bulk RNA-seq samples of freshly isolated total ASPCs, CD142⁺ and CD142⁻ ASPCs at different ages were first analysed using conventional log CPM normalisation as described above (Fig 2F and G, Appendix Figs S13, S14 and S15). In a second part, the analysis was performed on the data corrected for Age. More precisely, the data were normalised using the *Seurat* pipeline, and scaled for Age using the function `ScaleData()` (Fig 2H).

Additional analyses specific to CD142⁻ ASPCs co-cultured with KD Aregs

In a first analysis, CD142⁻ ASPCs receiving in a transwell assay WT Aregs, Aregs KD using si*Mgp*, si*F3*, si*Gdf10*, scrambled (scr) or with an empty well were analysed as described above in the “General method” section (Fig 4C, differential expression analysis result of

Fig 4D, Appendix Fig S22C, S24B and C, and S27A, differential expression analysis result of Appendix Fig S27B). As described in the manuscript, the samples clustered in two groups: CD142⁻ ASPCs co-cultured with “active Aregs” (wild type (WT) CD142⁺ ASPCs or CD142⁺ ASPCs treated with si*Gdf10* or scrambled (scr)) or CD142⁻ ASPCs co-cultured with “dysfunctional Aregs” (CD142⁺ ASPCs treated with si*Mgp*, si*F3*, or empty transwell (null)). Differential expression analysis was performed between these two groups and used to order the genes on the heatmaps (Fig 4D and Appendix Fig S27B).

In a second part, CD142⁺ and CD142⁻ ASPCs samples of cells post differentiation were integrated in the analysis. The heatmap of Fig 4E displays the Euclidean distance calculated on the first five principal components of the PCA (Appendix Fig S22D). The linear regression between the “white fat cell differentiation score” or “CD142⁺ score” (Appendix Table S1) and the gene expression of each gene (white fat cell differentiation score \sim log normalised gene expression of gene n or CD142⁺ score \sim log normalised gene expression of gene n) was calculated and the results are shown in Figs 4G and 5E, respectively. The volcano plots show the estimated slope (x -axis) versus the $-\log_{10}(P\text{-value})$, where the P -value for each term tests the null hypothesis that the coefficient is equal to zero.

All the different transcriptomic datasets are summarised in Appendix Table S2.

Comparison of various datasets (scRNA-seq, bulk RNA-seq, mass spectrometry)

The top CD142⁺ markers (Appendix Table S1) were compared across various datasets of freshly isolated CD142⁺ versus CD142⁻ ASPCs. Figure 1D displays the spearman correlation and the linear regression fitted to the logFC of the expression of these markers in freshly isolated CD142⁺ ASPCs versus CD142⁻ ASPCs of the different datasets by pairs. For bulk RNA-seq and mass spectrometry data, the logFC was defined as the log₂FC of freshly isolated CD142⁺ over CD142⁻ ASPCs. For the scRNA-seq, the logFC was defined as the average logFC across the logFC of the F3⁺ cluster over the rest of the cells calculated in the different datasets used for the integration described in the section “Integration of adult mouse subcutaneous adipose tissue”.

Statistical methods

The experiments were not randomised, and the investigators were not blinded in experiments. The paired Student's t -test was used to determine statistical differences between two groups, with the null hypothesis being that the two groups are equal. Multiple comparisons were corrected using false discovery rate (FDR) correction. When specified, one-way ANOVA followed by Tukey honest significant difference (HSD) *post hoc* correction was applied, the null hypothesis being defined so that the difference of means was zero. (Adjusted) * P value < 0.05, ** P value < 0.01, *** P value < 0.001 were considered statistically significant.

All boxplots display the mean as a dark band, the box shows the 25th and 75th percentiles, while the whiskers indicate the minimum and maximum data points in the considered dataset excluding outliers. All bar plots display the mean value, and the standard deviation from the mean as error bar.

Data availability

All raw and processed RNA-seq and proteomic data have been uploaded in ArrayExpress with the accession numbers: E-MTAB-10179 (<http://www.ebi.ac.uk/arrayexpress/experiments/E-MTAB-10179>), E-MTAB-10180 (<http://www.ebi.ac.uk/arrayexpress/experiments/E-MTAB-10180>), E-MTAB-10181 (<http://www.ebi.ac.uk/arrayexpress/experiments/E-MTAB-10181>), E-MTAB-10182 (<http://www.ebi.ac.uk/arrayexpress/experiments/E-MTAB-10182>), E-MTAB-10183 (<http://www.ebi.ac.uk/arrayexpress/experiments/E-MTAB-10183>) and E-MTAB-10184 (<http://www.ebi.ac.uk/arrayexpress/experiments/E-MTAB-10184>). Microscopy images are available upon request. Sample scripts used to process the data are available upon request.

Expanded View for this article is available online.

Acknowledgements

The authors thank W. Chen, G. van Mierlo and Judith F. Kribelbauer for constructive discussions and careful reading of the manuscript, R. Sarkis for her help for the adipogenic quantification of the *in vivo* plugs as well as C. Steiner for her assistance on the experiments. This research was supported by the Swiss National Science Foundation Grants (#31003A_162735, 31003A_182655 and CRSII5_186271), the Precision and Health-related Technologies Initiative Grants (PHRT #222, #307 and #502) and by institutional support from the Swiss Federal Institute of Technology in Lausanne (EPFL). The authors thank the EPFL Core Facilities: CPG (Centre de phéno génomique, especially Arnaud Legay), FCCF (Flow Cytometry Core Facility, especially Miguel Garcia), BIOP (Bioluminescence and Optics Platform, especially Olivier Buri and Romain Guet), PCF (Proteomics Core Facility, especially Romain Hamelin and Florence Armand), GECF (Gene Expression Core Facility, especially Bastien Mangeat). Open access funding provided by Ecole Polytechnique Fédérale de Lausanne.

Author contributions

Magda Zachara: Conceptualization; data curation; formal analysis; supervision; validation; investigation; visualization; methodology; writing – original draft; writing – review and editing. **Pernille Y Rainer:** Conceptualization; data curation; formal analysis; supervision; validation; investigation; visualization; methodology; writing – original draft; writing – review and editing.

Horia Hashimi: Conceptualization; data curation; formal analysis; validation; investigation; visualization; methodology; writing – original draft; writing – review and editing. **Julie M Russeil:** Methodology. **Daniel Alpern:** Investigation; methodology. **Radiana Ferrero:** Visualization; methodology.

Maria Litovchenko: Data curation; formal analysis. **Bart Deplancke:** Conceptualization; supervision; funding acquisition; writing – original draft; project administration; writing – review and editing.

Disclosure and competing interests statement

The authors declare that they have no conflict of interest.

References

- Alpern D, Gardeux V, Russeil J, Mangeat B, Meireles-Filho ACA, Breyse R, Hacker D, Deplancke B (2019) BRB-seq: ultra-affordable high-throughput transcriptomics enabled by bulk RNA barcoding and sequencing. *Genome Biol* 20: 71

- Andrews TS, Hemberg M (2019) M3Drop: dropout-based feature selection for scRNASeq. *Bioinformatics* 35: 2865–2867
- Atanassova P, Rancic G, Georgieva E (2012) Morphological characteristics of neonatal adipose tissue. *Folia Biol (Krakow)* 60: 41–43
- Bäck M, Aranyi T, Cancela ML, Carracedo M, Conceição N, Leftheriotis G, Macrae V, Martin L, Nitschke Y, Pasch A et al (2019) Endogenous calcification inhibitors in the prevention of vascular calcification: a consensus statement from the COST action EuroSoftCalcNet. *Front Cardiovasc Med* 5: 196
- Balmer JE, Blomhoff R (2002) Gene expression regulation by retinoic acid. *J Lipid Res* 43: 1773–1808
- Benjamini Y, Hochberg Y (1995) Controlling the false discovery rate: a practical and powerful approach to multiple testing. *J R Stat Soc B Methodol* 57: 289–300
- Berry DC, Noy N (2009) All-trans-retinoic acid represses obesity and insulin resistance by activating both peroxisome proliferation-activated receptor β/δ and retinoic acid receptor. *Mol Cell Biol* 29: 3286–3296
- Birsoy K, Berry R, Wang T, Ceyhan O, Tavazoie S, Friedman JM, Rodeheffer MS (2011) Analysis of gene networks in white adipose tissue development reveals a role for ETS2 in adipogenesis. *Development* 138: 4709–4719
- Bonet ML, Ribot J, Palou A (2012) Lipid metabolism in mammalian tissues and its control by retinoic acid. *Biochim Biophys Acta* 1821: 177–189
- Boney CM, Smith RM, Gruppuso PA (1998) Modulation of insulin-like growth factor I mitogenic signaling in 3T3-L1 preadipocyte differentiation*. *Endocrinology* 139: 1638–1644
- Burl RB, Ramseyer VD, Rondini EA, Pique-Regi R, Lee Y-H, Granneman JG (2018) Deconstructing adipogenesis induced by β 3-adrenergic receptor activation with single-cell expression profiling. *Cell Metab* 28: 300–309
- Camps J, Breuls N, Sifrim A, Giarratana N, Corvelyn M, Danti L, Grosemans H, Vanuytven S, Thiry I, Belicchi M et al (2020) Interstitial cell remodeling promotes aberrant adipogenesis in dystrophic muscles. *Cell Rep* 31: 107597
- Carberry AE, Colditz PB, Lingwood BE (2010) Body composition from birth to 4.5 months in infants born to non-obese women. *Pediatr Res* 68: 84–88
- Cho DS, Lee B, Doles JD (2019) Refining the adipose progenitor cell landscape in healthy and obese visceral adipose tissue using single-cell gene expression profiling. *Life Sci Alliance* 2: e201900561
- Chu AJ (2011) Tissue factor, blood coagulation, and beyond: an overview. *Int J Inflamm* 2011: 367284
- Cleal L, Aldea T, Chau Y-Y (2017) Fifty shades of white: understanding heterogeneity in white adipose stem cells. *Adipocyte* 6: 205–216
- Corvera S (2021) Cellular heterogeneity in adipose tissues. *Annu Rev Physiol* 83: 257–278
- Cristancho AG, Lazar MA (2011) Forming functional fat: a growing understanding of adipocyte differentiation. *Nat Rev Mol Cell Biol* 12: 722–734
- Dong H, Sun W, Shen Y, Baláz M, Balázová L, Ding L, Löffler M, Hamilton B, Klötting N, Blüher M et al (2022) Identification of a regulatory pathway inhibiting adipogenesis via RSPO2. *Nat Metab* 4: 90–105
- Dorfer V, Pichler P, Stranzl T, Stadlmann J, Taus T, Winkler S, Mechtler K (2014) MS Amanda, a universal identification algorithm optimized for high accuracy tandem mass spectra. *J Proteome Res* 13: 3679–3684
- Ferrero R, Rainer P, Deplancke B (2020) Toward a consensus view of mammalian adipocyte stem and progenitor cell heterogeneity. *Trends Cell Biol* 30: 937–950
- Fontaine DA, Davis DB (2016) Attention to background strain is essential for metabolic research: C57BL/6 and the International Knockout Mouse Consortium. *Diabetes* 65: 25–33
- Goldstein BJ, Scalia RG, Ma XL (2009) Protective vascular and myocardial effects of adiponectin. *Nat Rev Cardiol* 6: 27–35
- Gu W, Nowak WN, Xie Y, Le Bras A, Hu Y, Deng J, Issa Bhaloo S, Lu Y, Yuan H, Fidanis E et al (2019) Single-cell RNA-sequencing and metabolomics analyses reveal the contribution of perivascular adipose tissue stem cells to vascular remodeling. *Arterioscler Thromb Vasc Biol* 39: 2049–2066
- Han J, Lee J-E, Jin J, Lim JS, Oh N, Kim K, Chang S-I, Shibuya M, Kim H, Koh GY (2011) The spatiotemporal development of adipose tissue. *Development* 138: 5027–5037
- Hao Y, Hao S, Andersen-Nissen E, Mauck WM, Zheng S, Butler A, Lee MJ, Wilk AJ, Darby C, Zager M et al (2021) Integrated analysis of multimodal single-cell data. *Cell* 184: 3573–3587
- Harrington M, Pond-Tor S, Boney CM (2007) Role of epidermal growth factor and ErbB2 receptors in 3T3-L1 adipogenesis. *Obesity* 15: 563–571
- Hepler C, Gupta RK (2017) The expanding problem of adipose depot remodeling and postnatal adipocyte progenitor recruitment. *Mol Cell Endocrinol* 445: 95–108
- Hepler C, Shan B, Zhang Q, Henry GH, Shao M, Vishvanath L, Ghaben AL, Mobley AB, Strand D, Hon GC et al (2018) Identification of functionally distinct fibro-inflammatory and adipogenic stromal subpopulations in visceral adipose tissue of adult mice. *Elife* 7: e39636
- Hino J, Miyazawa T, Miyazato M, Kangawa K (2012) Bone morphogenetic protein-3b (BMP-3b) is expressed in adipocytes and inhibits adipogenesis as a unique complex. *Int J Obes (Lond)* 36: 725–734
- Hong KY, Bae H, Park I, Park D-Y, Kim KH, Kubota Y, Cho E-S, Kim H, Adams RH, Yoo O-J et al (2015) Perilipin+ embryonic preadipocytes actively proliferate along growing vasculatures for adipose expansion. *Development* 142: 2623–2632
- Hwang I, Kim JB (2019) Two faces of white adipose tissue with heterogeneous adipogenic progenitors. *Diabetes Metab J* 43: 752–762
- Kim DM, Choi H-R, Park A, Shin S-M, Bae K-H, Lee SC, Kim I-C, Kim WK (2013) Retinoic acid inhibits adipogenesis via activation of Wnt signaling pathway in 3T3-L1 preadipocytes. *Biochem Biophys Res Commun* 434: 455–459
- Kiselev VY, Kirschner K, Schaub MT, Andrews T, Yiu A, Chandra T, Natarajan KN, Reik W, Barahona M, Green AR et al (2017) SC3: consensus clustering of single-cell RNA-seq data. *Nat Methods* 14: 483–486
- Kong AT, Leprevost FV, Avtonomov DM, Mellacheruvu D, Nesvizhskii AI (2017) MSFragger: ultrafast and comprehensive peptide identification in mass spectrometry-based proteomics. *Nat Methods* 14: 513–520
- Kuri-Harcuch W (1982) Differentiation of 3T3-F442A cells into adipocytes is inhibited by retinoic acid. *Differentiation* 23: 164–169
- Lee JS, Park J-H, Kwon IK, Lim JY (2011) Retinoic acid inhibits BMP4-induced C3H10T1/2 stem cell commitment to adipocyte via downregulating Smad/p38MAPK signaling. *Biochem Biophys Res Commun* 409: 550–555
- Lee KY, Luong Q, Sharma R, Dreyfuss JM, Ussar S, Kahn CR (2019) Developmental and functional heterogeneity of white adipocytes within a single fat depot. *EMBO J* 38: e99291
- Li C, Li J, He F, Li K, Li X, Zhang Y (2020) Matrix Gla protein regulates adipogenesis and is serum marker of visceral adiposity. *Adipocyte* 9: 68–76
- Louveau I, Perruchot M-H, Bonnet M, Gondret F (2016) Invited review: pre- and postnatal adipose tissue development in farm animals: from stem cells to adipocyte physiology. *Animal* 10: 1839–1847
- Love MI, Huber W, Anders S (2014) Moderated estimation of fold change and dispersion for RNA-seq data with DESeq2. *Genome Biol* 15: 550
- MacDougald OA, Mandrup S (2002) Adipogenesis: forces that tip the scales. *Trends Endocrinol Metab* 13: 5–11

- McCarthy DJ, Chen Y, Smyth GK (2012) Differential expression analysis of multifactor RNA-Seq experiments with respect to biological variation. *Nucleic Acids Res* 40: 4288–4297
- Meissburger B, Perdikari A, Moest H, Müller S, Geiger M, Wolfrum C (2016) Regulation of adipogenesis by paracrine factors from adipose stromal-vascular fraction – a link to fat depot-specific differences. *Biochim Biophys Acta* 1861: 1121–1131
- Merrick D, Sakers A, Irgebay Z, Okada C, Calvert C, Morley MP, Percec I, Seale P (2019) Identification of a mesenchymal progenitor cell hierarchy in adipose tissue. *Science* 364: eaav2501
- Murray T, Russell TR (1980) Inhibition of adipose conversion in 3T3-L2 cells by retinoic acid. *J Supramol Struct* 14: 255–266
- Nguyen HP, Lin F, Yi D, Xie Y, Dinh J, Xue P, Sul HS (2021) Aging-dependent regulatory cells emerge in subcutaneous fat to inhibit adipogenesis. *Dev Cell* 56: 1437–1451.e3
- Nie B, Nie T, Hui X, Gu P, Mao L, Li K, Yuan R, Zheng J, Wang H, Li K et al (2017) Brown adipogenic reprogramming induced by a small molecule. *Cell Rep* 18: 624–635
- Petersen LC, Valentin S, Hedner U (1995) Regulation of the extrinsic pathway system in health and disease: the role of factor VIIa and tissue factor pathway inhibitor. *Thromb Res* 79: 1–47
- Plubell DL, Wilmarth PA, Zhao Y, Fenton AM, Minnier J, Reddy AP, Klimek J, Yang X, David LL, Pamir N (2017) Extended multiplexing of tandem mass tags (TMT) labeling reveals age and high fat diet specific proteome changes in mouse epididymal adipose tissue. *Mol Cell Proteomics* 16: 873–890
- Rappsilber J, Mann M, Ishihama Y (2007) Protocol for micro-purification, enrichment, pre-fractionation and storage of peptides for proteomics using StageTips. *Nat Protoc* 2: 1896–1906
- Reichert B, Yasmeen R, Jayakumar SM, Yang F, Thomou T, Alder H, Duester G, Maiseyeu A, Mihai G, Harrison EH et al (2011) Concerted action of aldehyde dehydrogenases influences depot-specific fat formation. *Mol Endocrinol* 25: 799–809
- Ritchie ME, Phipson B, Wu D, Hu Y, Law CW, Shi W, Smyth GK (2015) limma powers differential expression analyses for RNA-sequencing and microarray studies. *Nucleic Acids Res* 43: e47
- Robinson MD, McCarthy DJ, Smyth GK (2010) edgeR: a Bioconductor package for differential expression analysis of digital gene expression data. *Bioinformatics* 26: 139–140
- Rosen ED, Spiegelman BM (2014) What we talk about when we talk about fat. *Cell* 156: 20–44
- Sagara C, Takahashi K, Kagechika H, Takahashi N (2013) Molecular mechanism of 9-cis-retinoic acid inhibition of adipogenesis in 3T3-L1 cells. *Biochem Biophys Res Commun* 433: 102–107
- Salazarolivo LA, Castromunozledo F, Delagarza M, Kuriharcuch W (1994) Inhibition of 3T3 adipogenesis by retinoic acid is not mediated by cytoplasmic retinoic acid-binding protein. *Biochem Biophys Res Commun* 204: 257–263
- Sárvári AK, Van Hauwaert EL, Markussen LK, Gammelmark E, Marcher A-B, Ebbesen MF, Nielsen R, Brewer JR, Madsen JGS, Mandrup S (2021) Plasticity of epididymal adipose tissue in response to diet-induced obesity at single-nucleus resolution. *Cell Metab* 33: 437–453
- Schwalie PC, Dong H, Zachara M, Russeil J, Alpern D, Akkiche N, Caprara C, Sun W, Schlaudraff K-U, Soldati G et al (2018) A stromal cell population that inhibits adipogenesis in mammalian fat depots. *Nature* 559: 103–108
- Schwartz MW, Baskin DG, Bukowski TR, Kuijper JL, Foster D, Lasser G, Prunkard DE, Porte D Jr, Woods SC, Seeley RJ et al (1996) Specificity of leptin action on elevated blood glucose levels and hypothalamic neuropeptide Y gene expression in ob/ob mice. *Diabetes* 45: 531–535
- Shamsi F, Tseng Y-H, Kahn CR (2021) Adipocyte microenvironment: everybody in the neighborhood talks about the temperature. *Cell Metab* 33: 4–6
- Shao M, Hepler C, Zhang Q, Shan B, Vishvanath L, Henry GH, Zhao S, An YA, Wu Y, Strand DW et al (2021) Pathologic HIF1 α signaling drives adipose progenitor dysfunction in obesity. *Cell Stem Cell* 28: 685–701
- Spallanzani RG, Zemmour D, Xiao T, Jayewickreme T, Li C, Bryce PJ, Benoist C, Mathis D (2019) Distinct immunocyte-promoting and adipocyte-generating stromal components coordinate adipose tissue immune and metabolic tenors. *Sci Immunol* 4: eaaw3658
- Takahashi K, Uchida N, Kitanaka C, Sagara C, Imai M, Takahashi N (2015) Inhibition of ASCT2 is essential in all-trans retinoic acid-induced reduction of adipogenesis in 3T3-L1 cells. *FEBS Open Bio* 5: 571–578
- Takeda K, Sriram S, Chan XHD, Ong WK, Yeo CR, Tan B, Lee S-A, Kong KV, Hoon S, Jiang H et al (2016) Retinoic acid mediates visceral-specific adipogenic defects of human adipose-derived stem cells. *Diabetes* 65: 1164–1178
- Tratwal J, Bekri D, Boussema C, Sarkis R, Kunz N, Koliqi T, Rojas-Sutterlin S, Schyrr F, Tavakol DN, Campos V et al (2020) MarrowQuant across aging and aplasia: a digital pathology workflow for quantification of bone marrow compartments in histological sections. *Front Endocrinol* 11: 480
- Wang B, Fu X, Zhu M-J, Du M (2017) Retinoic acid inhibits white adipogenesis by disrupting GADD45A-mediated Zfp423 DNA demethylation. *J Mol Cell Biol* 9: 338–349
- Wang C, Pattabiraman N, Zhou JN, Fu M, Sakamaki T, Albanese C, Li Z, Wu K, Hult J, Neumeister P et al (2003) Cyclin D1 repression of peroxisome proliferator-activated receptor γ expression and transactivation. *Mol Cell Biol* 23: 6159–6173
- Yu G, Wang L-G, Han Y, He Q-Y (2012) clusterProfiler: an R package for comparing biological themes among gene clusters. *OMICS* 16: 284–287
- Zappia L, Oshlack A (2018) Clustering trees: a visualization for evaluating clusterings at multiple resolutions. *GigaScience* 7: giy083
- Zizola CF, Frey SK, Jitngarmkusol S, Kadereit B, Yan N, Vogel S (2010) Cellular retinol-binding protein type I (CRBP-I) regulates adipogenesis. *Mol Cell Biol* 30: 3412–3420



License: This is an open access article under the terms of the [Creative Commons Attribution-NonCommercial-NoDerivs](https://creativecommons.org/licenses/by-nc-nd/4.0/) License, which permits use and distribution in any medium, provided the original work is properly cited, the use is non-commercial and no modifications or adaptations are made.